

Polarization transfer and spin response functions in quasielastic (\vec{p}, \vec{n}) reactions at 346 MeV

T. Wakasa,^{1,*†} H. Sakai,¹ K. Hatanaka,² H. Okamura,^{1,‡} H. Otsu,^{1,§} S. Fujita,^{1,||} T. Nonaka,^{1,¶} T. Uesaka,^{1,**} Y. Satou,^{1,**} T. Ohnishi,¹ G. Yokoyama,^{1,††} S. Ishida,^{3,‡‡} N. Sakamoto,³ M. B. Greenfield,⁴ M. Ichimura,⁵ and K. Kawahigashi⁶

¹Department of Physics, University of Tokyo, Bunkyo, Tokyo 113-0033, Japan

²Research Center for Nuclear Physics, Osaka University, Ibaraki, Osaka 567-0047, Japan

³The Institute of Physical and Chemical Research, Wako, Saitama 351-0198, Japan

⁴Division of Natural Sciences, International Christian University, Mitaka, Tokyo 181-8585, Japan

⁵Institute of Physics, University of Tokyo, Komaba, Meguro, Tokyo 153-8902, Japan

⁶Department of Information Science, Kanagawa University, Hiratsuka, Kanagawa 259-1293, Japan

(Received 18 September 1998)

A complete set of polarization transfer coefficients has been measured for quasielastic (\vec{p}, \vec{n}) reactions on ^2H , ^6Li , ^{12}C , ^{40}Ca , and ^{208}Pb at a bombarding energy of 346 MeV and a laboratory scattering angle of 22° ($q_{\text{lab}} \approx 1.7 \text{ fm}^{-1}$). The spin-longitudinal R_L and spin-transverse R_T response functions are extracted within a framework of a plane-wave impulse approximation with eikonal and optimal factorization approximations. The theoretically expected enhancement of R_L/R_T is not observed. The observed R_L is consistent with the pionic enhanced R_L expected by random-phase approximation (RPA) calculations. On the contrary, a large excess of the observed R_T is found in comparison with R_T of the quasielastic electron scattering as well as of RPA calculations. This excess masks the effect of pionic correlations in R_L/R_T . The theoretical calculations are performed in a distorted-wave impulse approximation with RPA correlations, which indicates that the nuclear absorption effect depends on the spin direction. This spin-direction dependence is responsible in part for the excess of R_T . [S0556-2813(99)02306-7]

PACS number(s): 25.40.Kv, 24.70.+s

I. INTRODUCTION

The role of the pion (π) and rho meson (ρ) in the nuclear spin-isospin response functions is one of the most interesting subjects of nuclear physics. The spin-isospin-dependent residual interaction is often given by the $\pi + \rho + g'$ model [1]. In this model with a standard value of $g' = 0.6 - 0.7$, the spin-longitudinal ($\sigma \cdot \hat{q}$) interaction becomes moderately attractive for $q > 0.8 \text{ fm}^{-1}$, while the spin-transverse ($\sigma \times \hat{q}$) interaction remains repulsive for the wide range of q [1].

In 1982, Alberico *et al.* [1] theoretically pointed out that the attractive spin-longitudinal interaction should induce an enhancement and a softening (shift toward lower energy

transfer) of the spin-longitudinal response function R_L with respect to the free-response function in the quasielastic region for $q > 1 \text{ fm}^{-1}$. On the contrary, the repulsive spin-transverse interaction should induce a quenching and a hardening (shift toward higher energy transfer) of the spin-transverse response function R_T in the same region. The enhancement of R_L has attracted much interest in connection with both the precursor phenomena of the pion condensation [1] and the pion excess in the nucleus [2–6].

The Saclay [7–9] and Bates [10–13] groups have reported R_T of the quasielastic electron scattering at several momentum transfers. The quasielastic electron scattering is a good probe for the study of R_T because electrons can penetrate the entire nuclear volume with little distortion. However, it cannot probe R_L in a one-photon-exchange plane-wave Born approximation (PWBA).

The (\vec{p}, \vec{p}') and (\vec{p}, \vec{n}) reactions can probe both R_L and R_T , and a measurement of a complete set of polarization transfer coefficients allows us to extract them. Even though distortions in the nuclear mean field would reduce the expected collective effects, most calculations including these effects have suggested a significant enhancement of R_L relative to R_T [14,15].

In 1984, Carey *et al.* [16,17] reported a complete set of polarization transfer coefficients for the quasielastic (\vec{p}, \vec{p}') scattering from ^2H , Ca, and Pb at $T_p = 500 \text{ MeV}$. Many other experimental efforts [18–20] have been carried out to measure complete sets of polarization transfer coefficients for laboratory momentum transfer q_{lab} near the expected maximum of the attractive spin-longitudinal interaction ($q_{\text{lab}} \approx 1.7 \text{ fm}^{-1}$). Analyses of these measurements do not reveal the theoretically expected enhancement and softening

*Electronic address: wakasa@rcnp.osaka-u.ac.jp

†Present address: Research Center for Nuclear Physics, Osaka University, Osaka 567-0047, Japan.

‡Present address: Department of Physics, Saitama University, Saitama 338-8570, Japan.

§Present address: Department of Physics, Tohoku University, Miyagi 980-8578, Japan.

||Present address: O-arai Engineering Center, Power Reactor and Nuclear Fuel Development Corporation, Ibaraki 311-1393, Japan.

¶Present address: Toyota Central Research and Development Laboratories, Inc., Aichi 480-1192, Japan.

**Present address: The Institute of Physical and Chemical Research, Saitama 351-0198, Japan.

††Present address: Digital Equipment Corporation Japan, Tokyo 167-0043, Japan.

‡‡Present address: Soei International Patent Firm, Tokyo 104-0031, Japan.

of R_L . However, interpretation of these results is problematic [14,15] since the (\vec{p}, \vec{p}') reaction could not distinguish between the isoscalar and isovector spin-response functions.

Recently, measurements of a complete set of polarization transfer coefficients for quasielastic (\vec{p}, \vec{n}) reactions on ${}^2\text{H}$, ${}^{12}\text{C}$, and ${}^{40}\text{Ca}$ at $T_p=494$ MeV and scattering angles of 12.5° , 18° , and 27° were performed at LAMPF [21–23]. These measurements yielded pure-isovector R_L and R_T separately, which shows no evidence for an enhancement of R_L relative to R_T . The conclusion of these measurements is that there is a strong enhancement of R_T which masks the effect of pionic correlations in the ratio R_L/R_T . However, there are uncertainties in the extraction of R_L and R_T , such as ambiguities associated with distortion effects and the free NN t matrix.

In this paper, we present the measurements of a complete set of polarization transfer coefficients for quasielastic (\vec{p}, \vec{n}) reactions on ${}^2\text{H}$, ${}^6\text{Li}$, ${}^{12}\text{C}$, ${}^{40}\text{Ca}$, and ${}^{208}\text{Pb}$ at $T_p=346$ MeV and a laboratory scattering angle of $\theta_{\text{lab}}=22^\circ$ which corresponds to $q_{\text{lab}}=1.7$ fm $^{-1}$ at the quasielastic peak. The momentum transfer is very close to that of the (\vec{p}, \vec{p}') and (\vec{p}, \vec{n}) experiments performed at LAMPF [16,17,21–23]. However, the distortion in the nuclear mean field becomes minimum around a nucleon kinetic energy of 300 MeV. Furthermore, the free NN t -matrix components relevant to the measurement at $T_p=346$ MeV are significantly different from those at $T_p=494$ MeV.

The measured polarization transfer coefficients and cross sections are used to separate the cross sections into nonspin, spin-longitudinal, and spin-transverse polarized cross sections. The spin-response functions can be deduced from them within a framework of a plane-wave impulse approximation (PWIA) with eikonal and optimal factorization approximations. The spin-transverse response function is compared to that of the quasielastic electron scattering, which enables us in part to assess the assumption of the reaction mechanism. The comparison of the experimental R_L and R_T to the theoretical ones with random-phase approximation (RPA) correlations is also performed. Finally, the polarized cross sections, the cross sections associated with longitudinal and transverse spin transfers, are compared to those calculated in a distorted-wave impulse approximation (DWIA) employing RPA response functions.

II. EXPERIMENTAL METHODS

The data presented here were obtained with the neutron time-of-flight (NTOF) facility [24] at the Research Center for Nuclear Physics (RCNP), Osaka University. These data represent the measurement of a complete set of polarization transfer coefficients with the NTOF facility. Detailed descriptions concerning the NTOF facility and the neutron detection system can be found in Refs. [24–26]. In the following subsections, therefore, we present a brief description of the detector system and discuss experimental details relevant to the present experiment.

A. Polarized proton beam

A polarized proton beam was provided by the newly constructed high intensity polarized ion source (HIPIS) [27].

TABLE I. Direction of beam polarization produced by the superconducting solenoid magnets SOL1 and SOL2.

Beam polarization	SOL1	SOL2
S	off	on
N	off	off
L	on	off

The nuclear polarization state was toggled between the normal, reverse, and unpolarized states every 8 s in order to cancel out any geometrically associated false asymmetries that might be present in the experimental instruments. The polarized proton beam extracted from HIPIS was injected into the AVF cyclotron and was accelerated up to $T_p=59.7$ MeV. The RF frequency of the AVF cyclotron was 16.244 MHz, which yielded a beam-pulse period of 61.6 ns.

The beam pulsing device is positioned in the injection line from the AVF to ring cyclotrons. The beam pulse selection enables us to reduce the wraparound of slow neutrons from preceding beam pulses. In the present measurement, the beam pulses were selected to 1/9, which yielded a beam-pulse period of 554.1 ns.

The pulse-selected beam was injected into the main ring cyclotron and was accelerated up to $T_p=346$ MeV. The single-turn extraction was maintained during the experiment so as to keep the beam-pulse period as well as to prevent the depolarization of the horizontal component of the polarization vector coming from the multiturn extraction. The ratio of multiturn extracted protons relative to single-turn extracted protons was typically less than 0.1%. Thus the effects of the multiturn extraction were negligibly small.

B. Proton spin precession magnets

Two sets of superconducting solenoid magnets (SOL1 and SOL2) [24] were installed in the injection line from the AVF to ring cyclotrons. Each magnet can rotate the direction of the polarization vector from the normal into sideways directions. These solenoid magnets are separated by a bend angle of 45° , thus they allow the delivery of the beam to the main ring cyclotron with two different directions of the polarization vector in the horizontal plane. The spin precession angle in a dipole magnet with a 45° bend angle is about 85.8° for 59.7 MeV protons. In this manner, we can provide a beam whose polarization axis is either S (sideways), N (normal), or L (longitudinal) direction at the exit of SOL2 as shown in Table I.

C. Beam-line polarimeter

The single-turn extracted beam from the ring cyclotron was transported to the neutron experimental hall along the $N\phi$ beam line. The beam polarizations (S , N , L) were monitored with two beam-line polarimeters BLP1 and BLP2. BLP1 is located in the $N\phi$ beam line and BLP2 is positioned at the neutron experimental hall (see Fig. 1). These polarimeters are separated by a bend angle of 98° , thus the horizontal and vertical components of the polarization vector can be determined simultaneously.

Each polarimeter consists of four arms of collimated pairs of conjugate-angle plastic-scintillator telescopes. The polar-

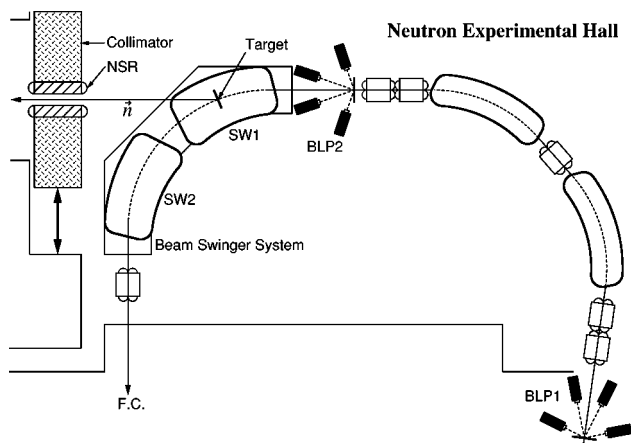


FIG. 1. Schematic layout of the neutron time-of-flight facility at RCNP (not to scale).

imetry is based on the analyzing power of the ${}^1\text{H}(\vec{p}, p){}^1\text{H}$ scattering. The elastically scattered and recoil protons are detected in coincidence with a conjugate-angle pair of plastic scintillators. The thicknesses of forward and backward plastic scintillators are 10 and 2 mm, respectively. The solid angle covered by a pair of scintillators is restricted to 2.1 msr by using a brass collimator installed in front of the backward scintillator. Both polarimeters use self-supporting CH_2 targets with a thickness of 2.5 mg/cm^2 as a hydrogen target.

The analyzing powers of BLP1 and BLP2 include the contribution of the quasielastic ($\vec{p}, 2p$) reaction on C whose analyzing power might be different from that of the free pp scattering. Thus the effective analyzing powers of BLP1 and BLP2 were calibrated as described in detail in Ref. [26]. The effective analyzing power at $T_p = 346 \text{ MeV}$ is 0.430. The statistical uncertainty is negligible and the systematic one is estimated to be ± 0.003 .

D. Beam swinger system

The beam swinger consists of two 45° bending C-shaped magnets (SW1 and SW2) with an orbit radius of 2.0 m (see Fig. 1). The gap and width of the pole are 10 and 40 cm, respectively.

The reaction angle of the (\vec{p}, \vec{n}) reaction can be varied by repositioning a target along the beam trajectory inside the pole gap, while the position of the neutron detector/polarimeter NPOL2 remains fixed along a 100 m neutron time-of-flight (TOF) tunnel. Therefore, both the reaction angle and the flight path length depend on the relative positions of the target and NPOL2 in the TOF tunnel.

E. Targets

A complete set of polarization transfer coefficients was measured for (\vec{p}, \vec{n}) reactions on CD_2 , enriched ${}^6\text{Li}$ ($\geq 99\%$ ${}^6\text{Li}$), natural C (98.9% ${}^{12}\text{C}$), natural Ca (96.9% ${}^{40}\text{Ca}$), and enriched ${}^{208}\text{Pb}$ ($\geq 99\%$ ${}^{208}\text{Pb}$). For the present purpose, the natural carbon and calcium can be regarded as ${}^{12}\text{C}$ and ${}^{40}\text{Ca}$, respectively. Targets with areal densities of 338 mg/cm^2 for CD_2 , 181 mg/cm^2 for ${}^6\text{Li}$, 260 mg/cm^2 for ${}^{12}\text{C}$, 359 mg/cm^2 for ${}^{40}\text{Ca}$, and 634 mg/cm^2 for ${}^{208}\text{Pb}$ were

used for the measurement of cross sections and analyzing powers. These target thicknesses correspond to about 1 MeV energy loss of incident protons which is slightly smaller than the intrinsic energy resolution of about 1.3 MeV of the NPOL2 system [24]. In the measurement of polarization transfer coefficients, thicker targets with areal densities of 662 mg/cm^2 for CD_2 , 376 mg/cm^2 for ${}^6\text{Li}$, 682 mg/cm^2 for ${}^{12}\text{C}$, 669 mg/cm^2 for ${}^{40}\text{Ca}$, and 1337 mg/cm^2 for ${}^{208}\text{Pb}$ were used to achieve reasonable statistical accuracy for the polarization transfer coefficients. These target thicknesses correspond to about 2 MeV energy loss of incident protons. Data for the ${}^2\text{H}(p, n)$ reaction were obtained from the cross-section weighted difference between the CD_2 and ${}^{12}\text{C}$ results.

F. Neutron spin rotation magnet

In order to measure the longitudinal component of the neutron polarization vector, a dipole magnet (NSR magnet) for rotating the direction of the neutron polarization vector was installed in the movable concrete shielding wall with a thickness of 1.5 m positioned at the entrance of the TOF tunnel (see Fig. 1). In the NSR magnet, the S' component of the neutron polarization vector is not affected, while the L' component is precessed into the N' component. In the measurement of the L' component of the neutron polarization, the NSR magnet was excited so that the precession angle became 90° for the neutron corresponding to the quasielastic peak. Because the precession angle in the magnetic field B_\perp is proportional to $1/\beta$, so that the lower energy neutrons were overprecessed (99.8° at $T_n = 195 \text{ MeV}$) and the higher energy neutrons were underprecessed (84.5° at $T_n = 315 \text{ MeV}$). Corrections for those over- and underprecessions were performed to account for the small amount of mixing between the N' and L' components.

This NSR magnet was also used for the measurement of the induced polarization P . In this case the N' component of the neutron polarization vector was precessed into the L' component.

G. Neutron detector/polarimeter NPOL2

The neutron detector/polarimeter NPOL2 [26] consists of six planes of two dimensionally position sensitive neutron detectors: four detectors of liquid scintillator BC519 and two detectors of plastic scintillator BC408. The liquid scintillator BC519 has a moderately high hydrogen-to-carbon ratio (H/C) of 1.7. This high H/C value is useful for neutron polarimetry where the $\vec{n} + p$ scattering in the scintillator provides the reaction to analyze the neutron polarization. All of the six neutron detectors have dimensions of $1 \times 1 \times 0.1 \text{ m}^3$. The position resolutions are about 6–10 cm and about 4–8 cm for liquid and plastic scintillators, respectively, depending on positions. Thin plastic scintillation detectors placed in front of each neutron detector are used to distinguish charged particles from neutrons.

An incident neutron energy is determined by the time-of-flight to a given neutron detector with respect to the cyclotron RF stop signal. A prominent γ -ray peak from the decay of π^0 produced in the target provides a time reference for the absolute timing calibration. Neutron kinetic energies are de-

terminated from the flight time. The overall energy resolutions in full width at half maximum, including target energy-loss contributions of about 1 MeV (for cross sections) and of about 2 MeV (for polarization transfer coefficients), are about 2 and 3 MeV for the cross section measurement and the polarization transfer measurement, respectively.

In the polarimetry mode of NPOL2, one of the five neutron detectors (all except for the last one) serves as a neutron polarization analyzer, and the following neutron detector acts as a catcher of doubly scattered neutrons or recoil protons. Time, position, and pulse-height information from both analyzer and catcher planes are used to kinematically discriminate the $\vec{n}+p$ events from the $\vec{n}+C$ events. This kinematical selection also provides a highly efficient filter against background events from cosmic rays, target γ rays, or the wrap-around of slow neutrons from preceding beam pulses. Neutron polarization is determined from the azimuthal distribution of the $\vec{n}+p$ events.

The magnitude and energy dependence of the effective analyzing powers of NPOL2 were determined with N -type polarized neutrons produced by the ${}^2\text{H}(\vec{p},\vec{n})pp$ reaction at $T_p=146, 228, 296, 346,$ and 392 MeV. The results are described in detail in Ref. [26]. For example, the effective analyzing powers of NPOL2 at $T_n=291$ MeV are 0.223 ± 0.010 and 0.132 ± 0.004 for (\vec{n},n) and (\vec{n},p) channels, respectively, where the uncertainties are the statistical ones. The systematic uncertainties come from the uncertainties both of incident proton polarization ($\sim 1\%$) and of polarization transfer coefficients for the ${}^2\text{H}(\vec{p},\vec{n})pp$ reaction (1–2%).

The neutron detection efficiency was determined by normalizing to neutron yields from the ${}^7\text{Li}(p,n){}^7\text{Be}(\text{g.s.}+0.43 \text{ MeV})$ reaction, which shows almost constant center-of-mass (c.m.) cross section of $\sigma_{\text{c.m.}}(0^\circ)=27.0 \pm 0.8$ mb/sr over the wide energy range of $T_p=80-795$ MeV [28]. This reaction was used at bombarding energies of $T_p=146, 228, 296, 346,$ and 392 MeV, which is sufficient to estimate the efficiencies spanning the neutron energy range necessary for the present data analysis. It is found that the detection efficiencies are almost independent of neutron kinetic energy, with a value of approximately 0.15 by combining all of the six neutron detectors. In the present analysis, the averaged value of the neutron detection efficiencies is used to deduce the cross section. A systematic uncertainty of the cross section normalization is estimated to be about 6% by considering the uncertainties both of the ${}^7\text{Li}$ cross section and of the target thickness.

III. DATA REDUCTION AND RESULTS

A. Coordinate system

The three orthogonal components of the outgoing neutron polarization $\mathbf{p}'=(p'_{S'}, p'_{N'}, p'_{L'})$ are related to the components of the incident proton polarization $\mathbf{p}=(p_S, p_N, p_L)$ through a set of polarization transfer coefficients $D_{ij}(i=S',N',L', j=S,N,L)$ according to

$$\begin{pmatrix} p'_{S'} \\ p'_{N'} \\ p'_{L'} \end{pmatrix} = \begin{bmatrix} D_{S'S} & 0 & D_{S'L} \\ 0 & D_{NN} & 0 \\ D_{L'S} & 0 & D_{L'L} \end{bmatrix} \begin{pmatrix} p_S \\ p_N \\ p_L \end{pmatrix} + \begin{pmatrix} 0 \\ P \\ 0 \end{pmatrix} \times \frac{1}{1+p_N A_y}. \quad (1)$$

This relation involves the complete set of polarization transfer coefficients allowed by parity conservation. The sideways (S), normal (N), and longitudinal (L) coordinates are defined in terms of the proton momentum \mathbf{k}_{lab} and the neutron momentum \mathbf{k}'_{lab} in the laboratory frame as $\hat{\mathbf{L}}=\hat{\mathbf{k}}_{\text{lab}}, \hat{\mathbf{L}}'=\hat{\mathbf{k}}'_{\text{lab}}, \hat{\mathbf{N}}=\hat{\mathbf{N}}'=(\mathbf{k}_{\text{lab}}\times\mathbf{k}'_{\text{lab}})/|\mathbf{k}_{\text{lab}}\times\mathbf{k}'_{\text{lab}}|, \hat{\mathbf{S}}=\hat{\mathbf{N}}\times\hat{\mathbf{L}},$ and $\hat{\mathbf{S}}'=\hat{\mathbf{N}}'\times\hat{\mathbf{L}}'.$

B. Data reduction

The measurement with the L -type beam provides $D_{L'L}$ and $D_{S'L}$, while the measurement with the S -type beam provides $D_{S'S}$ and $D_{L'S}$. In the present experiment, the L - and S -type beams have small S and L components, respectively. Thus we have obtained the polarization transfer coefficients associated with the sideways and longitudinal polarization components as follows.

When the SOL1 magnet is on, we assume the three orthogonal components of the polarization vector of protons and neutrons at the target position as $\mathbf{p}_1=(p_{1S}, 0, p_{1L})$ and $\mathbf{p}'_1=(p'_{1S'}, 0, p'_{1L'})$, respectively. The component of the polarization vector in the L - S plane can be rotated by an angle of 85.8° by switching off SOL1 and on SOL2. The resulting polarization vectors of protons and neutrons at the target position are $\mathbf{p}_2=(p_{2S}, 0, p_{2L})$ and $\mathbf{p}'_2=(p'_{2S'}, 0, p'_{2L'})$, respectively. The components of the polarization vectors are related to D_{ij} according to

$$p'_{1S'}=p_{1S}D_{S'S}+p_{1L}D_{S'L}, \quad (2a)$$

$$p'_{1L'}=p_{1S}D_{L'S}+p_{1L}D_{L'L}, \quad (2b)$$

$$p'_{2S'}=p_{2S}D_{S'S}+p_{2L}D_{S'L}, \quad (2c)$$

$$p'_{2L'}=p_{2S}D_{L'S}+p_{2L}D_{L'L}. \quad (2d)$$

Thus, the polarization transfer coefficients $D_{S'S}, D_{S'L}, D_{L'S},$ and $D_{L'L}$ are obtained as

$$D_{S'S}=\frac{p'_{1S'}p_{2L}-p'_{2S'}p_{1L}}{p_{1S}p_{2L}-p_{2S}p_{1L}}, \quad (3a)$$

$$D_{S'L}=-\frac{p'_{1S'}p_{2S}-p'_{2S'}p_{1S}}{p_{1S}p_{2L}-p_{2S}p_{1L}}, \quad (3b)$$

$$D_{L'S}=\frac{p'_{1L'}p_{2L}-p'_{2L'}p_{1L}}{p_{1S}p_{2L}-p_{2S}p_{1L}}, \quad (3c)$$

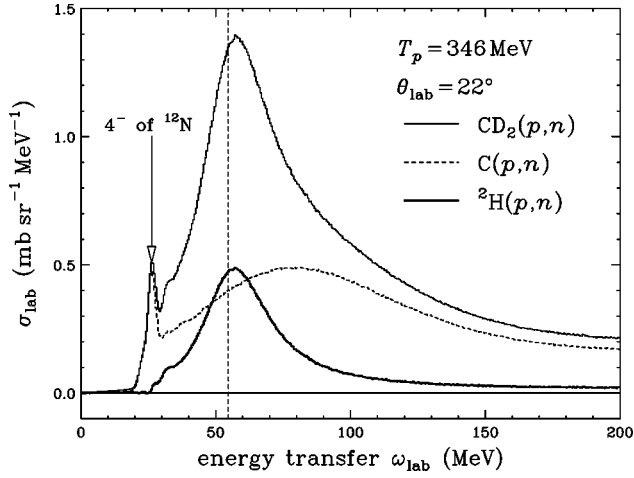


FIG. 2. Cross sections for (p,n) reactions on CD_2 (thin curve), ^{12}C (dashed curve), and ^2H (thick curve) obtained with the N -type polarized beam. A dashed vertical line marks the energy transfer for the free np scattering.

$$D_{L'L} = -\frac{p'_{1L}p'_{2S} - p'_{2L}p'_{1S}}{p_{1S}p_{2L} - p_{2S}p_{1L}}. \quad (3d)$$

Because the component of the polarization vector in the L - S plane can be rotated by an angle of 85.8° , the efficiency of measuring the polarization transfer coefficients is almost the same as that with pure S - and L -type beams.

The analyzing power A_y , induced polarization P , and polarization transfer coefficient D_{NN} are obtained with the N -type beam. An independent measurement of P is also performed with the unpolarized beam. The values of P obtained with polarized and unpolarized beams are consistent with each other within their statistical uncertainties.

In the actual experiment with the S - and L -type beams using the SOL1 and SOL2 magnets, the N -type component of the polarization vector was not zero and took a value typically less than 0.01. Likewise a minor component in the L - S plane of the polarization vector was observed for the measurement with the N -type beam. The effects of these minor components have been accounted for in all of the values reported here.

C. Observables for the $^2\text{H}(\vec{p},\vec{n})$ reaction

Observables for the $^2\text{H}(\vec{p},\vec{n})$ reaction were extracted by means of a cross section weighted subtraction of the $\text{C}(\vec{p},\vec{n})$ observables from the $\text{CD}_2(\vec{p},\vec{n})$ observables. Figure 2 shows a representative set of cross section spectra as a function of laboratory-frame energy transfer ω_{lab} . The $^2\text{H}(\vec{p},\vec{n})$ cross section was obtained from the $\text{CD}_2(\vec{p},\vec{n})$ and $\text{C}(\vec{p},\vec{n})$ reactions as

$$\sigma_{^2\text{H}} = (\sigma_{\text{CD}_2} - \sigma_{\text{C}})/2. \quad (4)$$

Polarization observables were obtained from

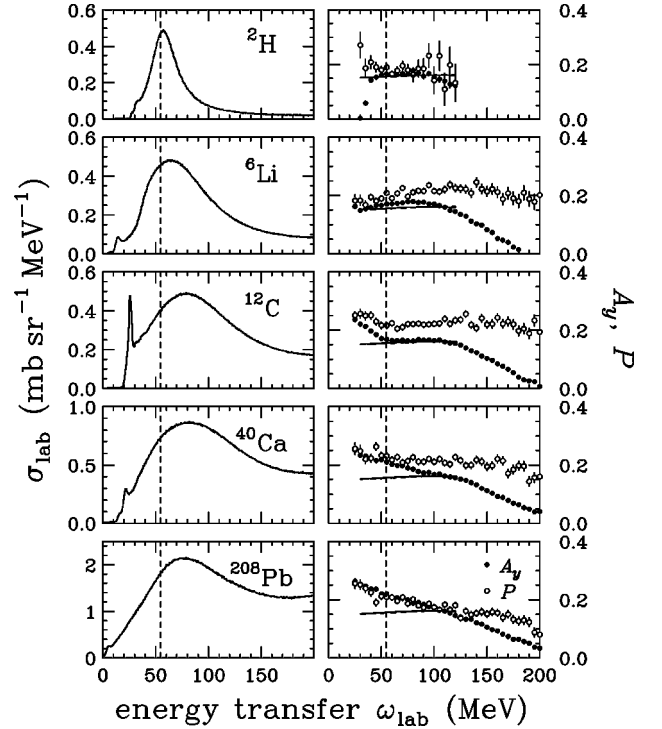


FIG. 3. Cross section, analyzing power, and induced polarization spectra for the ^2H , ^6Li , ^{12}C , ^{40}Ca , $^{208}\text{Pb}(\vec{p},\vec{n})$ reactions at $T_p = 346$ MeV and $\theta_{\text{lab}} = 22^\circ$. The cross section is binned in 0.5 MeV steps. The analyzing power and induced polarization are binned in 5 MeV steps. The dashed vertical lines mark the energy transfer for the free np scattering. The solid curves shown from 30 to 120 MeV represent the optimal-frame np values with the phase-shift solution of Bugg and Bryan [29]. The dashed curves are the values with the SP98 phase-shift solution of Arndt [30].

$$D_{^2\text{H}} = (D_{\text{CD}_2} - f_{\text{C}} D_{\text{C}}) / (1 - f_{\text{C}}), \quad (5)$$

where D represents one of the polarization observables D_{ij} , P , or A_y , and $f_{\text{C}} = \sigma_{\text{C}} / \sigma_{\text{CD}_2}$ is the carbon fraction of the CD_2 cross section. The carbon fraction was estimated by using the cross sections based on the target thicknesses and integrated beam current. The relative normalization was then adjusted to produce the best subtraction of the prominent peak corresponding to the 4^- state at $E_x = 4.2$ MeV in ^{12}N . The normalization factor varies its value from 0.99 to 1.01 for different polarization observables D . This variation might come from the uncertainty of the integrated beam current which is estimated to be about 2%.

D. Observables for quasielastic (\vec{p},\vec{n}) reactions

The cross section, analyzing power, and induced polarization for (\vec{p},\vec{n}) reactions on ^2H , ^6Li , ^{12}C , ^{40}Ca , and ^{208}Pb are presented in Fig. 3. Note that the analyzing power and induced polarization for ^2H are in fairly good agreement with each other around the quasielastic peak. This suggests that the quasielastic scattering on ^2H can be assumed as almost free np elastic scattering with little distortion (shadowing) effect. The quasielastic distributions for ^{12}C , ^{40}Ca ,

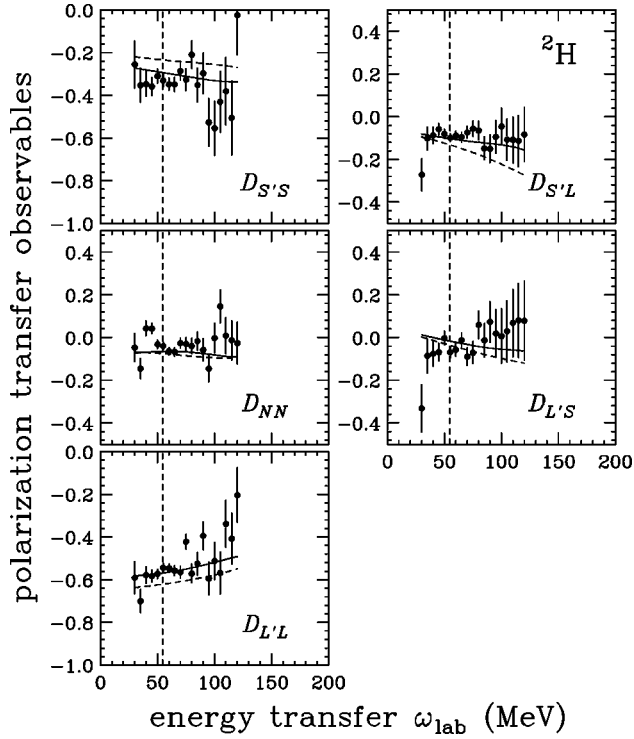


FIG. 4. Polarization transfer coefficients $D_{S'S}$, D_{NN} , $D_{L'L}$, $D_{S'L}$, and $D_{L'S}$ for the ${}^2\text{H}(\vec{p}, \vec{n})$ reaction at $T_p=346$ MeV and $\theta_{\text{lab}}=22^\circ$. The notations of the curves are the same as those in Fig. 3.

and ${}^{208}\text{Pb}$ peak at $\omega_{\text{lab}} \approx 80$ MeV, which is more than 20 MeV larger than that for the free np scattering.

The solid curves in Fig. 3 represent the corresponding free np values in the optimal frame with the phase-shift solution of Bugg and Bryan [29]. The dashed curves correspond to the values with the SP98 phase-shift solution of Arndt [30]. The optimal factorization approximation [31] was adopted to deduce these values. This approximation is valid only around the quasielastic peak. Thus optimal-frame free np values are shown only in the range of $\omega_{\text{lab}}=30$ –120 MeV. Note that the free np values correspond to the values in PWIA calculations without correlations. These optimal-frame free np values reproduce the experimentally obtained analyzing power reasonably well around the quasielastic peak.

The polarization transfer coefficients $D_{S'S}$, D_{NN} , $D_{L'L}$, $D_{S'L}$, and $D_{L'S}$ are presented in Figs. 4–8. The data here are binned in 5 MeV intervals. The uncertainties in the polarization transfer D_{NN} around the quasielastic peak are about 0.014 per 5-MeV bin, which should be compared to the uncertainties (0.024 per 10-MeV bin) in the similar measurement at LAMPF at $T_p=494$ MeV [21–23]. The dotted vertical lines mark the energy transfer for the free np scattering. The solid curves represent the optimal-frame free np values with the phase-shift solution of Bugg and Bryan [29]. The dashed curves correspond to the values with the SP98 phase-shift solution of Arndt [30]. Around the quasielastic peak, these optimal-frame free np values can reproduce the experimentally obtained D_{ij} values for nuclear targets fairly well except for D_{NN} . In the following, we deduce the experimental spin-response functions from these data, and compare

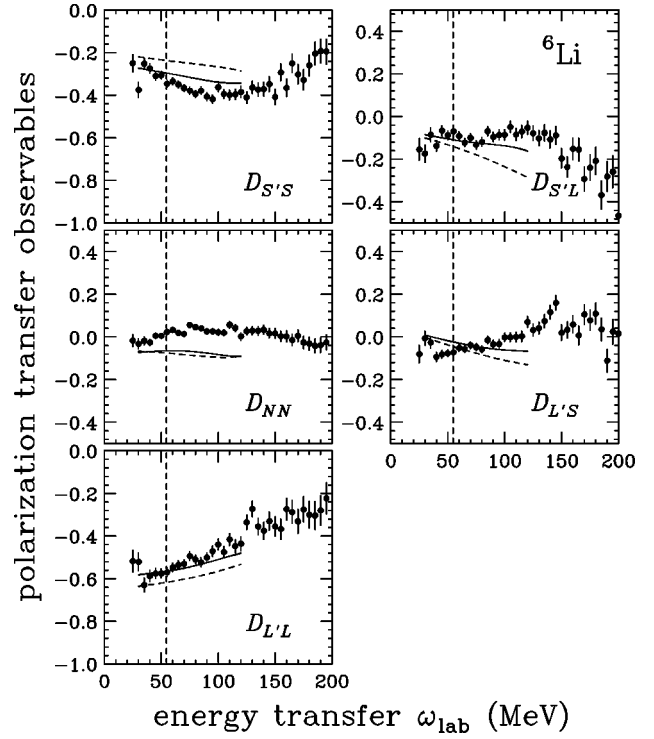


FIG. 5. Same as Fig. 4 but for the ${}^6\text{Li}(\vec{p}, \vec{n})$ reaction.

them to the spin-transverse response function of the quasielastic electron scattering and to the RPA response functions.

The data for ${}^{40}\text{Ca}$ presented in Figs. 3 and 7 are tabulated in Tables II and III, respectively. The data for all five targets shown in Figs. 3–8 are available with the Physics Auxiliary Publication Service of the American Institute of Physics [32].

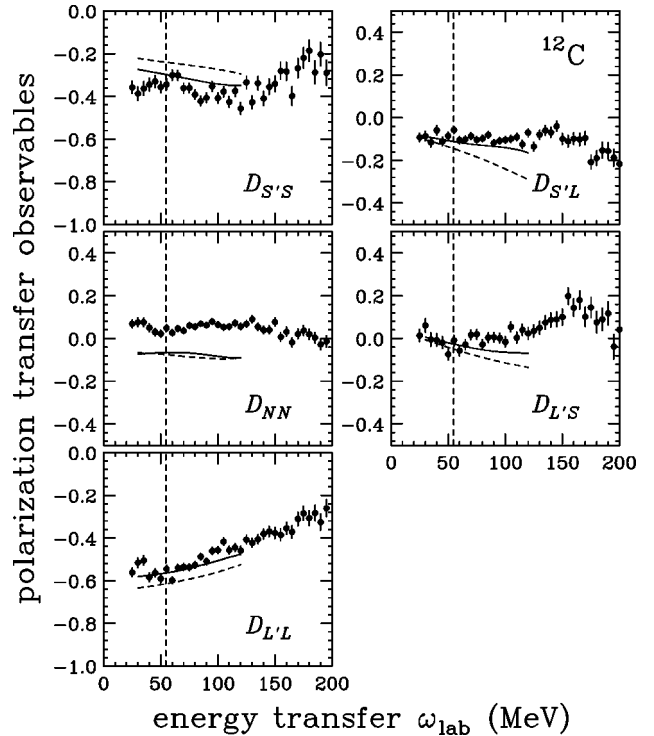
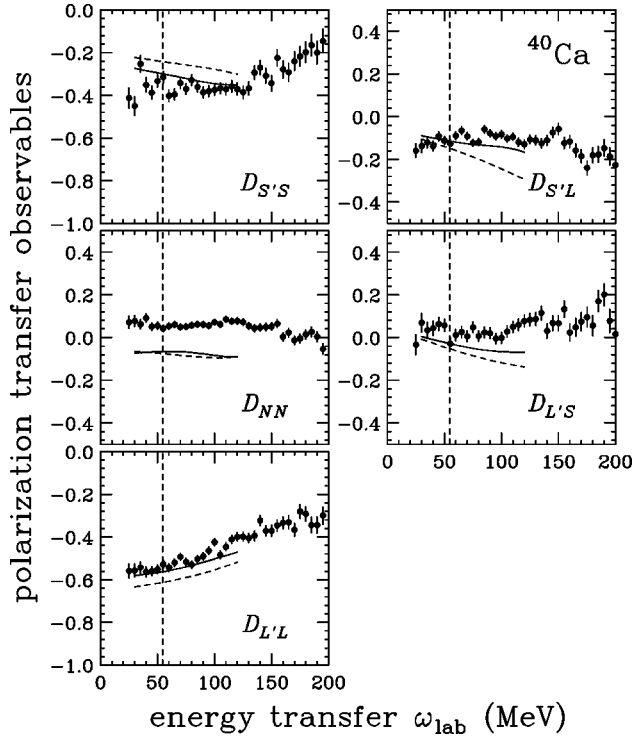


FIG. 6. Same as Fig. 4 but for the ${}^{12}\text{C}(\vec{p}, \vec{n})$ reaction.


 FIG. 7. Same as Fig. 4 but for the $^{40}\text{Ca}(\vec{p}, \vec{n})$ reaction.

IV. DEFINITION OF EXPERIMENTAL SPIN-RESPONSE FUNCTIONS

A. Coordinate system

The momentum transfer in the nucleon-nucleus (NA) center-of-mass (c.m.) system is given by

$$\mathbf{q} = \mathbf{k}' - \mathbf{k}, \quad (6)$$

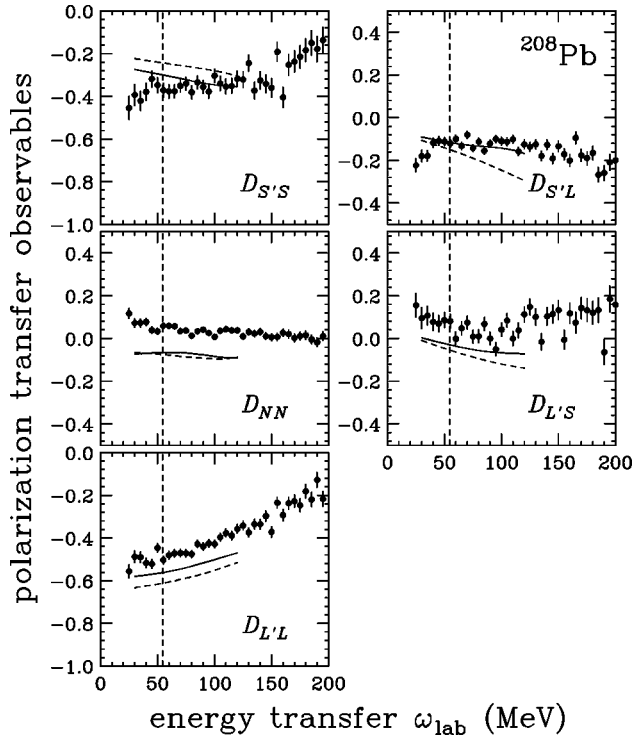

 FIG. 8. Same as Fig. 4 but for the $^{208}\text{Pb}(\vec{p}, \vec{n})$ reaction.

TABLE II. The cross section (laboratory), analyzing power, and induced polarization for the $^{40}\text{Ca}(\vec{p}, \vec{n})$ reaction at 346 MeV and $\theta_{\text{lab}} = 22^\circ$. The uncertainties are from statistical uncertainty only.

ω_{lab} (MeV)	σ_{lab} (mb sr $^{-1}$ MeV $^{-1}$)	A_y	P
25.0	0.2600 ± 0.0007	0.250 ± 0.004	0.256 ± 0.020
30.0	0.3131 ± 0.0008	0.233 ± 0.003	0.247 ± 0.018
35.0	0.4176 ± 0.0009	0.230 ± 0.003	0.220 ± 0.016
40.0	0.5104 ± 0.0010	0.221 ± 0.003	0.222 ± 0.014
45.0	0.5968 ± 0.0011	0.215 ± 0.003	0.263 ± 0.013
50.0	0.6746 ± 0.0012	0.218 ± 0.002	0.232 ± 0.012
55.0	0.7351 ± 0.0012	0.210 ± 0.002	0.231 ± 0.011
60.0	0.7818 ± 0.0012	0.202 ± 0.002	0.217 ± 0.011
65.0	0.8171 ± 0.0013	0.198 ± 0.002	0.227 ± 0.010
70.0	0.8407 ± 0.0013	0.197 ± 0.002	0.209 ± 0.010
75.0	0.8553 ± 0.0013	0.190 ± 0.002	0.213 ± 0.010
80.0	0.8624 ± 0.0013	0.185 ± 0.002	0.226 ± 0.010
85.0	0.8595 ± 0.0013	0.177 ± 0.002	0.211 ± 0.010
90.0	0.8530 ± 0.0013	0.172 ± 0.002	0.211 ± 0.010
95.0	0.8369 ± 0.0013	0.174 ± 0.002	0.221 ± 0.010
100.0	0.8156 ± 0.0013	0.167 ± 0.002	0.211 ± 0.010
105.0	0.7885 ± 0.0012	0.168 ± 0.002	0.220 ± 0.010
110.0	0.7588 ± 0.0012	0.162 ± 0.002	0.207 ± 0.010
115.0	0.7284 ± 0.0012	0.159 ± 0.002	0.203 ± 0.010
120.0	0.6930 ± 0.0012	0.156 ± 0.002	0.227 ± 0.011
125.0	0.6576 ± 0.0011	0.151 ± 0.002	0.216 ± 0.011
130.0	0.6242 ± 0.0011	0.147 ± 0.002	0.199 ± 0.011
135.0	0.5949 ± 0.0011	0.139 ± 0.003	0.199 ± 0.012
140.0	0.5659 ± 0.0010	0.132 ± 0.003	0.217 ± 0.012
145.0	0.5409 ± 0.0010	0.119 ± 0.003	0.211 ± 0.013
150.0	0.5180 ± 0.0010	0.111 ± 0.003	0.194 ± 0.013
155.0	0.4988 ± 0.0010	0.103 ± 0.003	0.197 ± 0.013
160.0	0.4813 ± 0.0010	0.092 ± 0.003	0.220 ± 0.014
165.0	0.4685 ± 0.0010	0.089 ± 0.003	0.214 ± 0.014
170.0	0.4536 ± 0.0009	0.078 ± 0.003	0.170 ± 0.015
175.0	0.4467 ± 0.0009	0.068 ± 0.003	0.184 ± 0.015
180.0	0.4398 ± 0.0009	0.063 ± 0.003	0.197 ± 0.015
185.0	0.4337 ± 0.0009	0.053 ± 0.003	0.195 ± 0.016
190.0	0.4324 ± 0.0009	0.048 ± 0.003	0.143 ± 0.016
195.0	0.4279 ± 0.0009	0.039 ± 0.003	0.156 ± 0.017
200.0	0.4288 ± 0.0009	0.040 ± 0.003	0.160 ± 0.018

where \mathbf{k} and \mathbf{k}' are the momenta of the incident and outgoing nucleons in the NA c.m. frame, respectively. Then the NA c.m. coordinate system (q, n, p) can be defined as

$$\hat{\mathbf{q}} = \frac{\mathbf{q}}{|\mathbf{q}|}, \quad (7a)$$

$$\hat{\mathbf{n}} = \frac{\mathbf{k} \times \mathbf{k}'}{|\mathbf{k} \times \mathbf{k}'|}, \quad (7b)$$

$$\hat{\mathbf{p}} = \hat{\mathbf{q}} \times \hat{\mathbf{n}}. \quad (7c)$$

TABLE III. Polarization transfer coefficients for the $^{40}\text{Ca}(\vec{p}, \vec{n})$ reaction at 346 MeV and $\theta_{\text{lab}}=22^\circ$. The uncertainties are from statistical uncertainty only.

ω_{lab} (MeV)	D_{NN}	$D_{S'S}$	$D_{L'L}$	$D_{L'S}$	$D_{S'L}$
25.0	0.072 ± 0.029	-0.413 ± 0.047	-0.559 ± 0.032	-0.034 ± 0.047	-0.159 ± 0.032
30.0	0.077 ± 0.026	-0.450 ± 0.044	-0.557 ± 0.030	0.069 ± 0.044	-0.138 ± 0.030
35.0	0.062 ± 0.022	-0.253 ± 0.038	-0.543 ± 0.026	0.033 ± 0.038	-0.122 ± 0.026
40.0	0.091 ± 0.020	-0.352 ± 0.034	-0.564 ± 0.023	0.043 ± 0.034	-0.138 ± 0.023
45.0	0.050 ± 0.018	-0.388 ± 0.031	-0.560 ± 0.021	0.063 ± 0.031	-0.092 ± 0.021
50.0	0.055 ± 0.017	-0.334 ± 0.029	-0.551 ± 0.020	0.057 ± 0.029	-0.113 ± 0.020
55.0	0.041 ± 0.016	-0.315 ± 0.027	-0.528 ± 0.019	-0.029 ± 0.027	-0.127 ± 0.019
60.0	0.053 ± 0.015	-0.402 ± 0.026	-0.543 ± 0.018	0.011 ± 0.026	-0.089 ± 0.018
65.0	0.060 ± 0.015	-0.396 ± 0.026	-0.521 ± 0.018	0.025 ± 0.026	-0.065 ± 0.018
70.0	0.049 ± 0.014	-0.342 ± 0.025	-0.493 ± 0.017	0.006 ± 0.025	-0.092 ± 0.017
75.0	0.050 ± 0.014	-0.370 ± 0.025	-0.517 ± 0.017	0.047 ± 0.025	-0.123 ± 0.017
80.0	0.057 ± 0.014	-0.329 ± 0.025	-0.530 ± 0.017	0.007 ± 0.025	-0.120 ± 0.017
85.0	0.062 ± 0.014	-0.360 ± 0.025	-0.504 ± 0.017	0.023 ± 0.025	-0.059 ± 0.017
90.0	0.060 ± 0.014	-0.387 ± 0.025	-0.491 ± 0.017	0.020 ± 0.025	-0.078 ± 0.017
95.0	0.056 ± 0.014	-0.381 ± 0.025	-0.465 ± 0.017	-0.005 ± 0.025	-0.092 ± 0.017
100.0	0.072 ± 0.014	-0.375 ± 0.026	-0.424 ± 0.018	-0.001 ± 0.026	-0.083 ± 0.018
105.0	0.062 ± 0.014	-0.367 ± 0.026	-0.484 ± 0.018	0.028 ± 0.026	-0.102 ± 0.018
110.0	0.085 ± 0.014	-0.371 ± 0.027	-0.446 ± 0.019	0.049 ± 0.027	-0.094 ± 0.019
115.0	0.076 ± 0.015	-0.359 ± 0.028	-0.411 ± 0.019	0.060 ± 0.028	-0.120 ± 0.019
120.0	0.078 ± 0.015	-0.370 ± 0.029	-0.400 ± 0.020	0.077 ± 0.029	-0.130 ± 0.020
125.0	0.073 ± 0.015	-0.386 ± 0.030	-0.399 ± 0.021	0.083 ± 0.030	-0.107 ± 0.021
130.0	0.054 ± 0.016	-0.367 ± 0.031	-0.405 ± 0.021	0.086 ± 0.031	-0.112 ± 0.021
135.0	0.043 ± 0.016	-0.294 ± 0.032	-0.394 ± 0.022	0.114 ± 0.032	-0.125 ± 0.022
140.0	0.046 ± 0.017	-0.270 ± 0.034	-0.323 ± 0.023	0.030 ± 0.034	-0.111 ± 0.023
145.0	0.049 ± 0.018	-0.308 ± 0.035	-0.372 ± 0.024	0.068 ± 0.035	-0.074 ± 0.024
150.0	0.052 ± 0.018	-0.344 ± 0.036	-0.371 ± 0.026	0.067 ± 0.036	-0.058 ± 0.026
155.0	0.064 ± 0.019	-0.225 ± 0.038	-0.346 ± 0.027	0.132 ± 0.038	-0.124 ± 0.027
160.0	0.003 ± 0.019	-0.279 ± 0.040	-0.334 ± 0.028	0.023 ± 0.040	-0.117 ± 0.028
165.0	0.023 ± 0.020	-0.292 ± 0.042	-0.331 ± 0.030	0.048 ± 0.042	-0.158 ± 0.030
170.0	-0.014 ± 0.021	-0.240 ± 0.044	-0.366 ± 0.031	0.095 ± 0.046	-0.240 ± 0.033
180.0	0.014 ± 0.022	-0.198 ± 0.049	-0.293 ± 0.035	0.056 ± 0.048	-0.181 ± 0.035
185.0	0.026 ± 0.023	-0.165 ± 0.050	-0.345 ± 0.036	0.170 ± 0.050	-0.177 ± 0.036
190.0	0.004 ± 0.023	-0.200 ± 0.053	-0.345 ± 0.038	0.201 ± 0.052	-0.147 ± 0.038
195.0	-0.054 ± 0.024	-0.145 ± 0.055	-0.300 ± 0.040	0.077 ± 0.054	-0.186 ± 0.041
200.0	-0.010 ± 0.025	-0.203 ± 0.058	-0.266 ± 0.042	0.016 ± 0.057	-0.227 ± 0.043

B. Optimal factorization in PWIA

The (p, n) unpolarized double differential cross section I in the NA laboratory frame can be separated into four polarized cross sections ID_i as

$$I = ID_0 + ID_q + ID_n + ID_p, \quad (8)$$

where D_i are the polarization observables introduced by Bleszynski *et al.* [33]. In PWIA with eikonal and optimal factorization approximations, ID_i are expressed as

$$ID_0 = 8CK(2J_A + 1)N_{\text{eff}}(|A^\eta|^2 R_0^- + |C_2^\eta|^2 R_n^-), \quad (9a)$$

$$ID_n = 8CK(2J_A + 1)N_{\text{eff}}(|B^\eta|^2 R_n^- + |C_1^\eta|^2 R_0^-), \quad (9b)$$

$$ID_q = 8CK(2J_A + 1)N_{\text{eff}}(|E^\eta|^2 R_q^- + |D_1^\eta|^2 R_p^-), \quad (9c)$$

$$ID_p = 8CK(2J_A + 1)N_{\text{eff}}(|F^\eta|^2 R_p^- + |D_2^\eta|^2 R_q^-), \quad (9d)$$

where C is the transformation factor defined below, K is the kinematical factor, J_A is the target spin, N_{eff} is the effective neutron number, $A^\eta - F^\eta$ are the components of the optimal-frame t matrix, and R_i^- are the nuclear response functions defined in the next subsection. The formalism to derive Eq. (9) is given in Ref. [31]. The isospin degree of freedom neglected in Ref. [31] is properly accounted for in Eq. (9).

The transformation factor C in Eq. (9) is required to obtain R_i^- defined by the intrinsic (internal) states of the target and the residual A -body system. It is given by [34]

$$C = \frac{d\Omega d\omega}{d\Omega_{\text{lab}} d\omega_{\text{lab}}} \frac{d\omega_{\text{int}}}{d\omega} = \frac{\sin \theta_{\text{c.m.}} \sqrt{S_{NA}}}{\sin \theta_{\text{lab}} M_T^*} \quad (10)$$

with

$$\omega_{\text{int}} = M_T^* - M_T, \quad (11)$$

where $d\Omega$ and $d\Omega_{\text{lab}}$ ($d\omega$ and $d\omega_{\text{lab}}$) are the solid angles (energy transfers) in the NA c.m. and laboratory frames, respectively, $\theta_{\text{c.m.}}$ and θ_{lab} are the scattering angles in the NA c.m. and laboratory frames, respectively, s_{NA} is the Mandelstam parameter of the NA system, and M_T and M_T^* are the invariant masses of the target and of the residual A -body system, respectively.

The kinematical factor K is given by [31]

$$K = \frac{\mu_i \mu_f}{(2\pi)^2} \frac{|\mathbf{k}'|}{|\mathbf{k}|} \frac{1}{2(2J_A + 1)}, \quad (12)$$

where μ_i and μ_f are the relativistic reduced energies of initial and final states, respectively.

The optimal-frame t matrix t^η has the form

$$t^\eta = (t_0^\eta + t_n^\eta \sigma_{0n} + t_q^\eta \sigma_{0q} + t_p^\eta \sigma_{0p}) \boldsymbol{\tau}_0 \cdot \boldsymbol{\tau}_1, \quad (13)$$

with components

$$t_0^\eta = A^\eta + C_2^\eta \sigma_{1n}, \quad (14a)$$

$$t_n^\eta = B^\eta \sigma_{1n} + C_1^\eta, \quad (14b)$$

$$t_q^\eta = E^\eta \sigma_{1q} + D_1^\eta \sigma_{1p}, \quad (14c)$$

$$t_p^\eta = F^\eta \sigma_{1p} + D_2^\eta \sigma_{1q}, \quad (14d)$$

where σ_{0i} and σ_{1i} are the Pauli spin matrices for the projectile and target nucleons projected onto the direction i , and $\boldsymbol{\tau}_0$ and $\boldsymbol{\tau}_1$ are the isospin of the projectile and target nucleons, respectively.

C. Theoretical definition of spin-response functions

The *normalized* spin-response function is theoretically defined by the intrinsic states of the target ($|I\rangle$) and the residual A -body system ($|F\rangle$) as

$$R_i^\mu(q, \omega_{\text{int}}) = \frac{1}{\mathcal{N}} \frac{1}{2J_A + 1} \sum_T \times \sum_F \left\langle \left\langle F \left| \sum_{j=1}^A \boldsymbol{\tau}_j^\mu(\boldsymbol{\sigma}_j)_i \exp(-i\mathbf{q} \cdot \mathbf{r}_{j;\text{int}}) \right| I \right\rangle \right\rangle^2 \times \delta(\omega_{\text{int}} - (E_{\text{int}}^F - E_{\text{int}}^I)). \quad (15)$$

\mathcal{N} depends on the isospin operator $\boldsymbol{\tau}_j^\mu$ as

$$\mathcal{N} = \begin{cases} 2N & \text{for } \boldsymbol{\tau}_j^\mu = \boldsymbol{\tau}_j^- \equiv \frac{\boldsymbol{\tau}_j^x - i\boldsymbol{\tau}_j^y}{\sqrt{2}}, \\ N+Z & \text{for } \boldsymbol{\tau}_j^\mu = \boldsymbol{\tau}_j^0 \equiv \boldsymbol{\tau}_j^z, \\ 2Z & \text{for } \boldsymbol{\tau}_j^\mu = \boldsymbol{\tau}_j^+ \equiv \frac{\boldsymbol{\tau}_j^x + i\boldsymbol{\tau}_j^y}{\sqrt{2}}, \end{cases} \quad (16)$$

where N and Z are neutron and proton numbers of the target nucleus, respectively.

The spin-response function R_i^μ is normalized as

TABLE IV. Effective bombarding energies $T_{\text{lab}}^{\text{eff}}$ and effective c.m. NN scattering angles $\theta_{\text{c.m.}}^{\text{eff}}$ for the $^{12}\text{C}(\vec{p}, \vec{n})$ and $^{40}\text{Ca}(\vec{p}, \vec{n})$ reactions at $T_p = 346$ MeV and $\theta_{\text{lab}} = 22^\circ$.

ω_{lab} (MeV)	$^{12}\text{C}(\vec{p}, \vec{n})$		$^{40}\text{Ca}(\vec{p}, \vec{n})$	
	$T_{\text{lab}}^{\text{eff}}$ (MeV)	$\theta_{\text{c.m.}}^{\text{eff}}$ (deg)	$T_{\text{lab}}^{\text{eff}}$ (MeV)	$\theta_{\text{c.m.}}^{\text{eff}}$ (deg)
30.0	372	46.2	373	46.1
60.0	340	47.8	341	47.8
90.0	302	51.1	301	51.1
120.0	259	56.4	259	56.5

$$\int_0^\infty R_i^\mu(q, \omega_{\text{int}}) d\omega_{\text{int}} \rightarrow 1 \quad \text{for } q \rightarrow \infty. \quad (17)$$

D. NN t matrix in optimal frame

The charge-exchange NN t matrix t^{NN} in the NN c.m. frame is expressed as [35]

$$t^{NN} = (A + B\sigma_{0n}\sigma_{1n} + C(\sigma_{0n} + \sigma_{1n}) + E\sigma_{0q}\sigma_{1q} + F\sigma_{0p}\sigma_{1p}) \boldsymbol{\tau}_0 \cdot \boldsymbol{\tau}_1. \quad (18)$$

The optimal-frame t matrix t^η is related to t^{NN} by the transformation [31]

$$t^\eta = J(\eta) \hat{R}(\eta) t^{NN}, \quad (19)$$

where $J(\eta)$ is the Jacobian (Möller factor) and $\hat{R}(\eta)$ is the relativistic spin rotation matrix.

The optimal-frame NN t matrix obtained from Eq. (19) is a function of the Mandelstam parameters s_{eff} and t_{eff} . The effective laboratory bombarding energy $T_{\text{lab}}^{\text{eff}} (= s_{\text{eff}}/2m_N - 2m_N)$ and the effective c.m. scattering angle $\theta_{\text{c.m.}}^{\text{eff}}$ are determined from these parameters. Some typical values for the $^{12}\text{C}(\vec{p}, \vec{n})$ and $^{40}\text{Ca}(\vec{p}, \vec{n})$ reactions in the present cases are shown in Table IV, in which the effective laboratory bombarding energies vary about 110 MeV. This variation gives rise to important consequences if the NN t matrix is strongly energy dependent. The squared t -matrix components in the optimal frame are displayed in Fig. 9 for the $^{12}\text{C}(\vec{p}, \vec{n})$ case. The mixing between R_q^- and R_p^- seen in Eq. (9) is negligible because the components D_1^η and D_2^η are very small. For the present case, $|D_1^\eta|^2/|E^\eta|^2 \approx |D_2^\eta|^2/|F^\eta|^2 < 0.01$. Note that both ID_0 and ID_n in Eq. (9) are insensitive to the spin-scalar response function R_0^- because of $|A^\eta|^2 \ll |C_2^\eta|^2$ and $|C_1^\eta|^2 \ll |B^\eta|^2$. Inversely, it is very hard to obtain R_0^- reliably. Therefore, we will evaluate only the spin-dependent response functions.

E. Definition of ‘‘experimental’’ spin-response functions

The relationship between ID_i and R_i^- in Eq. (9) can be simplified by considering the relative magnitude between the t -matrix components in the optimal frame.

First, the polarized cross sections ID_q and ID_p are directly related to R_q^- and R_p^- , respectively, as

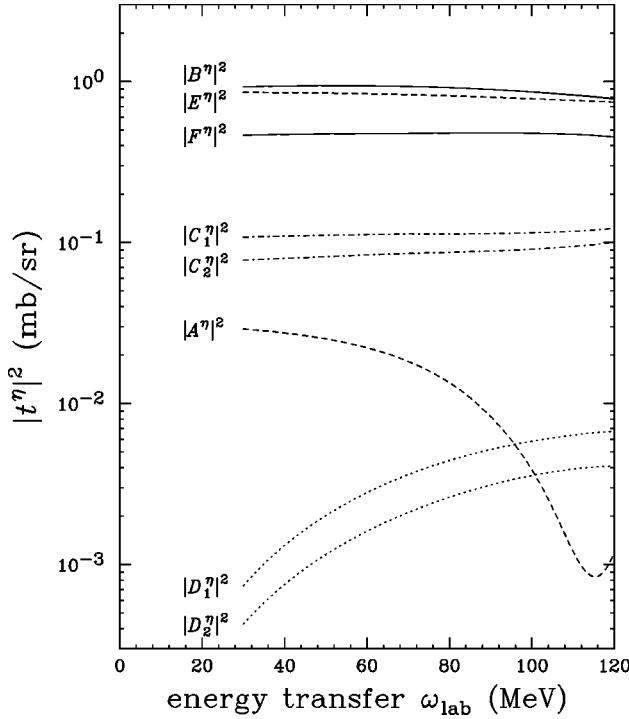


FIG. 9. Squared t -matrix components in the optimal frame with the Bugg and Bryan [29] phase-shift solution. The components are derived according to the optimal-frame kinematics for the $^{12}\text{C}(\vec{p}, \vec{n})$ reaction at $T_p = 346$ MeV and $\theta_{\text{lab}} = 22^\circ$.

$$ID_q = 8CK(2J_A + 1)N_{\text{eff}}|E^\eta|^2 R_q^-, \quad (20a)$$

$$ID_p = 8CK(2J_A + 1)N_{\text{eff}}|F^\eta|^2 R_p^-, \quad (20b)$$

where the small contributions of D_1^η and D_2^η are neglected.

Second, from Eq. (9), ID_n can be written as

$$ID_n = 8CK(2J_A + 1)N_{\text{eff}}(|B^\eta|^2 + |C_1^\eta|^2) \times \left\{ 1 + \frac{|C_1^\eta|^2}{|B^\eta|^2 + |C_1^\eta|^2} \frac{R_0^- - R_n^-}{R_n^-} \right\} R_n^-. \quad (21)$$

For example, $|C_1^\eta|^2/(|B^\eta|^2 + |C_1^\eta|^2)$ is typically about 0.05 for the $^{12}\text{C}(\vec{p}, \vec{n})$ reaction in the present kinematical condition (see Fig. 9). Furthermore, the absolute magnitude of $(R_0^- - R_n^-)/R_n^-$ is expected to be less than 1. Thus the second term in the braces in Eq. (21) can be neglected. As a result, ID_n is directly related to R_n^- as

$$ID_n = 8CK(2J_A + 1)N_{\text{eff}}(|B^\eta|^2 + |C_1^\eta|^2)R_n^-. \quad (22)$$

From Eqs. (20) and (22), the *experimental* spin-response functions can be defined as

$$R_q^- = \frac{ID_q}{8CK(2J_A + 1)N_{\text{eff}}|E^\eta|^2}, \quad (23a)$$

$$R_p^- = \frac{ID_p}{8CK(2J_A + 1)N_{\text{eff}}|F^\eta|^2}, \quad (23b)$$

$$R_n^- = \frac{ID_n}{8CK(2J_A + 1)N_{\text{eff}}(|B^\eta|^2 + |C_1^\eta|^2)}. \quad (23c)$$

V. EXTRACTION OF EXPERIMENTAL SPIN-RESPONSE FUNCTIONS

The experimental spin-response functions can be extracted by using Eq. (23). For this purpose, the experimental polarization transfer coefficients D_{ij} should be transformed into the polarization observables D_i , and the effective neutron number N_{eff} should be calculated. Furthermore, it is very important to select a reliable free NN t matrix which is used to obtain the optimal-frame t matrix by using Eq. (19).

A. Polarization observables

The polarization observables D_i are related to the NA laboratory-frame polarization transfer coefficients D_{ij} according to [31]

$$D_0 = \frac{1}{4} [1 + D_{NN} + (D_{S'S} + D_{L'L}) \cos \alpha_1 + (D_{L'S} - D_{S'L}) \sin \alpha_1], \quad (24a)$$

$$D_n = \frac{1}{4} [1 + D_{NN} - (D_{S'S} + D_{L'L}) \cos \alpha_1 - (D_{L'S} - D_{S'L}) \sin \alpha_1], \quad (24b)$$

$$D_q = \frac{1}{4} [1 - D_{NN} + (D_{S'S} - D_{L'L}) \cos \alpha_2 - (D_{L'S} + D_{S'L}) \sin \alpha_2], \quad (24c)$$

$$D_p = \frac{1}{4} [1 - D_{NN} - (D_{S'S} - D_{L'L}) \cos \alpha_2 + (D_{L'S} + D_{S'L}) \sin \alpha_2], \quad (24d)$$

where $\alpha_1 \equiv \theta_{\text{lab}} + \Omega$ and $\alpha_2 \equiv 2\theta_p - \theta_{\text{lab}} - \Omega$. The angle θ_p represents the angle between the incident beam direction and the unit vector $\hat{\mathbf{p}}$ defined in Eq. (7), and the relativistic spin rotation angle Ω is given by [36]

$$\tan(\theta_{\text{c.m.}} - \theta_{\text{lab}} - \Omega) = \frac{\sin \theta_{\text{c.m.}}}{\gamma(\cos \theta_{\text{c.m.}} + \beta/\beta_{\text{c.m.}})}, \quad (25)$$

where $\beta_{\text{c.m.}}$ is the velocity of the NA c.m. frame relative to that of the NA laboratory frame, β is the velocity of the outgoing nucleon in the NA c.m. frame, and $\gamma \equiv 1/\sqrt{1 - \beta^2}$.

B. Effective neutron number

The effective neutron number N_{eff} acts as an overall attenuation factor which is given in the eikonal approximation as

$$N_{\text{eff}}(T_{\text{lab}}) = \frac{N}{A} \int_0^\infty 2\pi b db n(b) \exp[-n(b)\tilde{\sigma}_{NN}(T_{\text{lab}})], \quad (26)$$

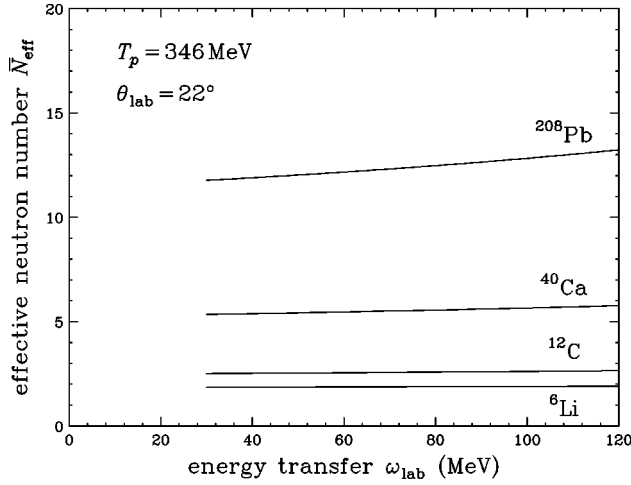


FIG. 10. Effective neutron numbers for the quasielastic (\vec{p}, \vec{n}) reactions on ${}^6\text{Li}$, ${}^{12}\text{C}$, ${}^{40}\text{Ca}$, and ${}^{208}\text{Pb}$ at $T_p = 346$ MeV and $\theta_{\text{lab}} = 22^\circ$.

where T_{lab} is the nucleon kinetic energy in the NA laboratory frame, b is the impact parameter, $\tilde{\sigma}_{NN}(T_{\text{lab}})$ is the total NN cross section in the nuclear medium, and

$$n(b) = \int_{-\infty}^{\infty} dz \rho_A(\sqrt{z^2 + b^2}). \quad (27)$$

The nuclear density ρ_A is taken from Ref. [37]. The in-medium total cross section is calculated by the method of Smith and Bozoian as [38]

$$\tilde{\sigma}_{NN}(T_{\text{lab}}) = \frac{2m_N}{k} \times 0.6T_{\text{lab}}. \quad (28)$$

N_{eff} , in principle, depends on both the incident proton and the outgoing neutron kinetic energies. Thus we account for this energy dependence by taking an average value as

$$\bar{N}_{\text{eff}} = \frac{N_{\text{eff}}(T_p) + N_{\text{eff}}(T_n)}{2}, \quad (29)$$

where T_p and T_n are incident proton and outgoing neutron kinetic energies, respectively.

The results are shown in Fig. 10 for the the present quasielastic (\vec{p}, \vec{n}) reactions on ${}^6\text{Li}$, ${}^{12}\text{C}$, ${}^{40}\text{Ca}$, and ${}^{208}\text{Pb}$ at $T_p = 346$ MeV and $\theta_{\text{lab}} = 22^\circ$. Around the quasielastic peak at $\omega_{\text{lab}} \approx 80$ MeV, the \bar{N}_{eff} values are 2.6 and 5.6 for ${}^{12}\text{C}$ and for ${}^{40}\text{Ca}$, respectively. Note that the use of the free total cross section of 32.5 mb at $T_p = 400$ MeV gives smaller $N_{\text{eff}}(T_p)$ values of 2.1 and 3.8 for ${}^{12}\text{C}$ and ${}^{40}\text{Ca}$, respectively [39].

The effective neutron number may also be estimated from the results of DWIA and PWIA calculations as [40]

$$\bar{N}_{\text{eff}}(\omega_{\text{lab}}) = N \frac{I^{\text{DW}}(\omega_{\text{lab}})}{I^{\text{PW}}(\omega_{\text{lab}})}, \quad (30)$$

where N is the target neutron number, and I^{DW} and I^{PW} are the unpolarized cross sections in DWIA and PWIA calculations, respectively. A brief description of DWIA calculations

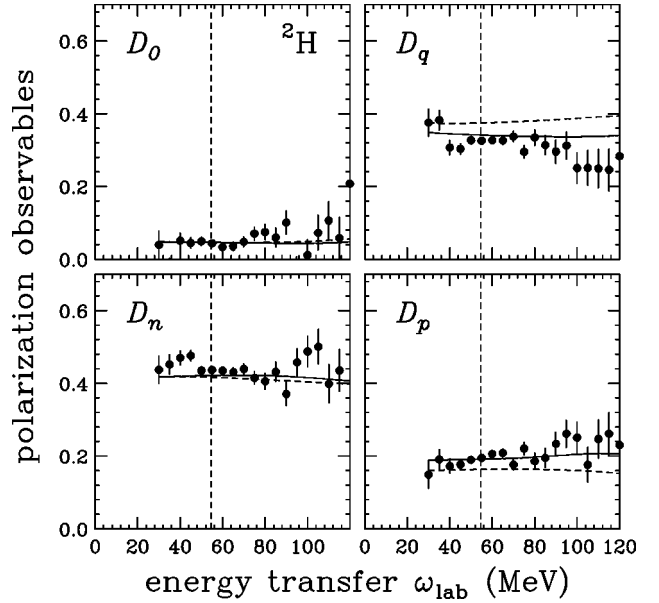


FIG. 11. Polarization observables for the ${}^2\text{H}(\vec{p}, \vec{n})$ reaction compared to optimal-frame np values. The solid and dashed curves represent the optimal-frame np values with the Bugg and Bryan phase shift [29] and with the SP98 phase shift [30], respectively. The dashed vertical lines mark the energy transfer for the free np scattering.

will be given in Sec. IX. The calculations were performed for ${}^{12}\text{C}$ and ${}^{40}\text{Ca}$ with the RPA response functions employing $(g'_{NN}, g'_{N\Delta}, g'_{\Delta\Delta}) = (0.6, 0.3, 0.5)$ and $m^*(r=0) = 0.7m_N$ [see Eq. (36)]. The results are $\bar{N}_{\text{eff}} = 2.7$ and 5.2 for ${}^{12}\text{C}$ and for ${}^{40}\text{Ca}$, respectively, around the quasielastic peak. Thus the uncertainty of \bar{N}_{eff} is estimated to be about 10%. In the following discussions, we use \bar{N}_{eff} for N_{eff} .

C. Comparison to ${}^2\text{H}(p, n)$ data

The data of the ${}^2\text{H}(\vec{p}, \vec{n})$ reaction provide a valuable check on the accuracy of the free NN t matrix derived from various phase-shift solutions as demonstrated in Ref. [22]. The polarization observables for ${}^2\text{H}$ are plotted in Fig. 11 along with the corresponding free np values in the optimal frame derived from the phase-shift solution of Bugg and Bryan [29] and from the SP98 phase-shift solution of Arndt [30]. In the region around the quasielastic peak, both solutions agree fairly well with the experimentally obtained observables D_0 and D_n . However, the solution of Bugg and Bryan reproduces better the observables D_q and D_p which are connected with R_q^- and R_p^- , respectively. The difference between these two phase-shift solutions can be further assessed by taking the ratio $D_q/D_p \approx |E^\eta|^2/|F^\eta|^2$, and the results are shown in Fig. 12. The ratios obtained from the Bugg and Bryan solution (solid curve) are close to the experimentally deduced ratios, while the values from the Arndt solution (dashed curve) are larger than the corresponding experimental values. Thus we have employed the Bugg and Bryan solution to extract the spin-response functions.

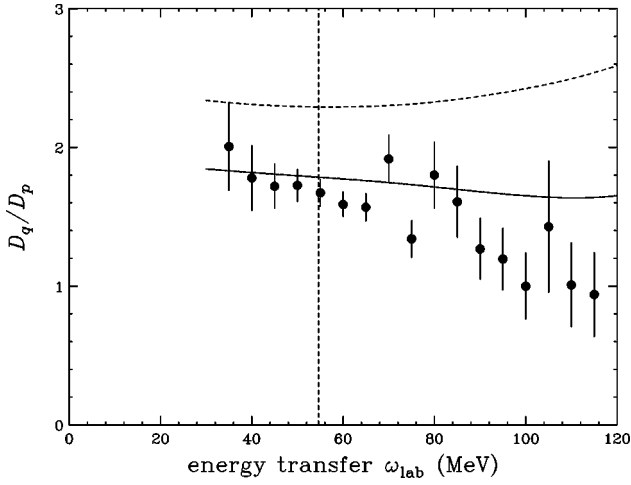


FIG. 12. Ratio of polarization observables D_q/D_p for the ${}^2\text{H}(\vec{p}, \vec{n})$ reaction at $T_p = 346$ MeV and $\theta_{\text{lab}} = 22^\circ$. The solid and dashed curves represent the ratio of the optimal-frame np values with the Bugg and Bryan phase shift [29] and with the SP98 phase shift [30], respectively. The dashed vertical line marks the energy transfer for the free np scattering.

VI. RESULTS OF EXPERIMENTAL SPIN-RESPONSE FUNCTIONS

A. Spin-response functions for ${}^2\text{H}$

Figure 13 shows the spin-response functions R_q^- , R_n^- , and R_p^- for ${}^2\text{H}$. We have used Eq. (23) to deduce these response functions in PWIA with $N_{\text{eff}} = 1$ (no absorption). Two spin-transverse response functions R_n^- and R_p^- can be independently determined experimentally. Because the n direction is identical to the p direction, R_n^- should be equal to R_p^- . The experimental R_n^- values are consistent with the

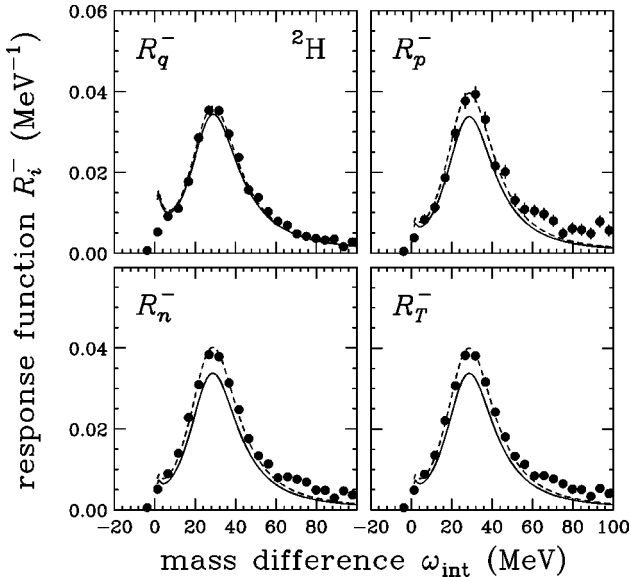


FIG. 13. The spin-response functions R_q^- , R_n^- , R_p^- , and R_T^- for the ${}^2\text{H}(\vec{p}, \vec{n})$ reaction at $T_p = 346$ MeV and $\theta_{\text{lab}} = 22^\circ$. The solid curves are the theoretical predictions from Itabashi, Aizawa, and Ichimura [41]. The dashed curves represent the calculations renormalized by $N_i = 1.06, 1.19, 1.17,$ and 1.18 for R_q^- , R_n^- , R_p^- , and R_T^- , respectively.

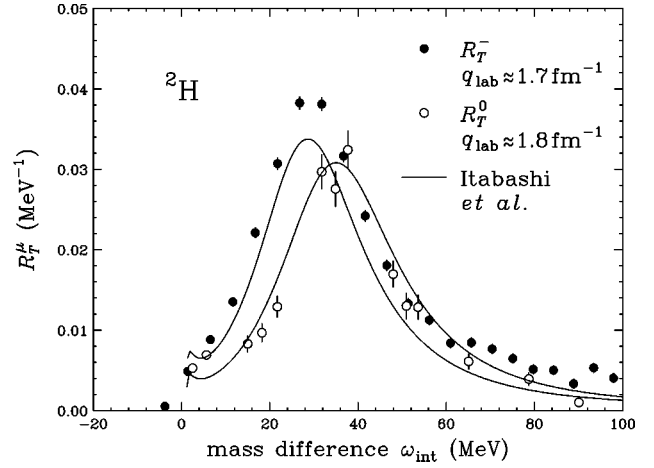


FIG. 14. The experimental spin-transverse response function R_T^- (filled circles) for the ${}^2\text{H}(\vec{p}, \vec{n})$ reactions at $T_p = 346$ MeV and $\theta_{\text{lab}} = 22^\circ$ ($q_{\text{lab}} \approx 1.7 \text{ fm}^{-1}$). The open circles are R_T^0 of the quasielastic electron scattering on ${}^2\text{H}$ at $E_0 = 233.1$ MeV and $\theta_{\text{lab}} = 134.5^\circ$ ($q_{\text{lab}} \approx 1.8 \text{ fm}^{-1}$) [42]. The solid curves are the theoretical predictions from Itabashi, Aizawa, and Ichimura [41].

corresponding R_p^- values, which shows the high reliability of our measurements as well as of the optimal-frame t matrix used in the present analysis. In this paper we set the spin-longitudinal R_L^- and spin-transverse R_T^- response functions as

$$R_L^- = R_q^-, \quad (31a)$$

$$R_T^- = \frac{R_n^- + R_p^-}{2}. \quad (31b)$$

The result of R_T^- is also shown in Fig. 13.

Recently, Itabashi, Aizawa, and Ichimura [41] calculated the response functions associated with the ${}^2\text{H}(\vec{p}, \vec{n})$ reaction, including the final-state interaction between two protons. The results are shown in Fig. 13 with the solid curves. The theoretical calculation reproduces both the magnitude and the shape of the spin-longitudinal response function fairly well, while the magnitude of the spin-transverse response functions is somewhat underestimated.

The spin-transverse response function R_T^0 of the quasielastic electron scattering on ${}^2\text{H}$ at $E_0 = 233.1$ MeV and $\theta_{\text{lab}} = 134.5^\circ$ ($q_{\text{lab}} \approx 1.8 \text{ fm}^{-1}$) has been reported by Dytman *et al.* [42]. The definition of R_T^0 of the quasielastic electron scattering is described in detail in Sec. VII. The result is compared with the present (\vec{p}, \vec{n}) spin-transverse response function R_T^- in Fig. 14, in which the theoretical calculations by Itabashi, Aizawa, and Ichimura at $q_{\text{lab}} \approx 1.7$ and 1.8 fm^{-1} are shown by the solid curves. Note that the contribution from the meson exchange current (MEC) to R_T^0 of the (e, e') scattering, which is neglected in the theoretical calculation, is expected to be small by about 5% [42]. The (e, e') spin-transverse response function agrees fairly well with the theoretical calculation. On the contrary, the (\vec{p}, \vec{n}) spin-transverse response function is systematically larger than both the (e, e') one and the theoretical calculation.

We introduce the normalization factor N_i in Eq. (23) as

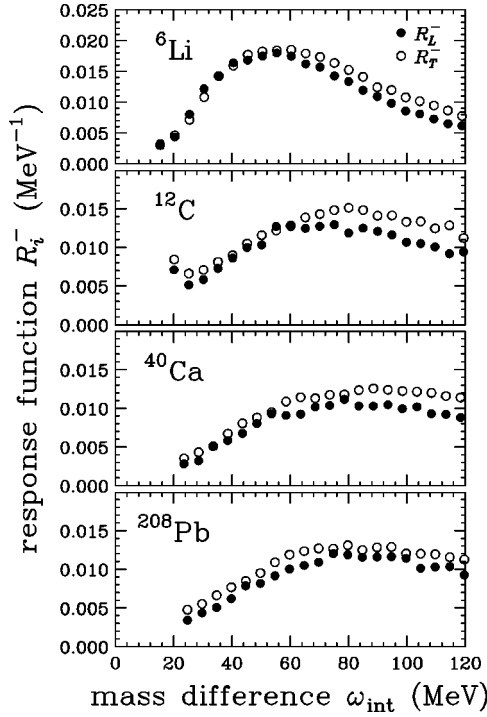


FIG. 15. The spin-longitudinal R_L^- and spin-transverse R_T^- response functions for (\vec{p}, \vec{n}) reactions on ${}^6\text{Li}$, ${}^{12}\text{C}$, ${}^{40}\text{Ca}$, and ${}^{208}\text{Pb}$ at $T_p = 346$ MeV and $\theta_{\text{lab}} = 22^\circ$.

$$R_q^- = \frac{1}{N_q} \frac{ID_q}{8CK(2J_A + 1)N_{\text{eff}}|E^\eta|^2}, \quad (32a)$$

$$R_p^- = \frac{1}{N_p} \frac{ID_p}{8CK(2J_A + 1)N_{\text{eff}}|F^\eta|^2}, \quad (32b)$$

$$R_n^- = \frac{1}{N_n} \frac{ID_n}{8CK(2J_A + 1)N_{\text{eff}}(|B^\eta|^2 + |C_1^\eta|^2)}. \quad (32c)$$

The N_i values have been adjusted so that the experimental spin-response functions are reproduced by the theoretical ones around the quasielastic peak. They are 1.06, 1.19, and 1.17 for N_q , N_n , and N_p , respectively.

There might be some origins of N_i . The experimental ID_i has uncertainties coming both from the cross section normalization (6%) and from the polarization observables D_i (2%). The ambiguity of the magnitude of the optimal-frame t matrix is estimated to be about 10%. Furthermore, there are uncertainties for the reaction mechanisms such as the shadowing effect since we deduced R_i^- on the assumption of $N_{\text{eff}} = 1$. Thus the obtained N_i values can be explained by considering these uncertainties.

B. Spin-response functions for nuclear targets

The spin-longitudinal R_L^- and spin-transverse R_T^- response functions for ${}^6\text{Li}$, ${}^{12}\text{C}$, ${}^{40}\text{Ca}$, and ${}^{208}\text{Pb}$ have been deduced by using Eq. (32), and the results are shown in Fig. 15. The results for ${}^{12}\text{C}$, ${}^{40}\text{Ca}$, and ${}^{208}\text{Pb}$ are very similar to each other. This is not surprising if we consider the remarkable similarity between their polarization transfer coefficients.

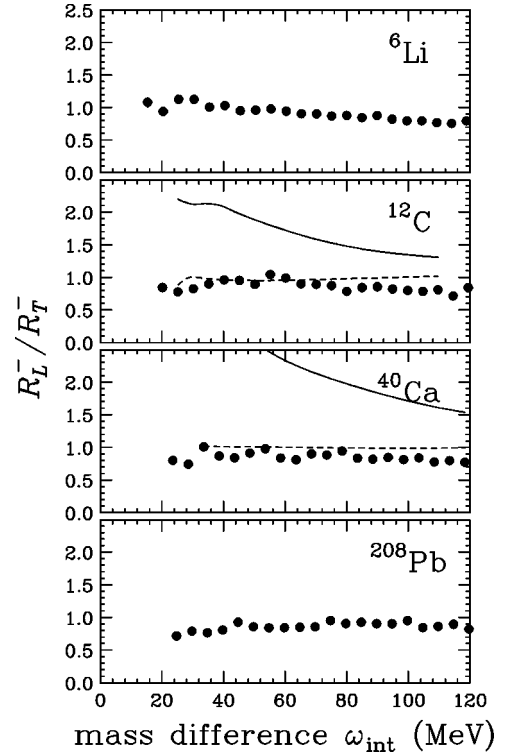


FIG. 16. The ratios R_L^-/R_T^- for the ${}^6\text{Li}$, ${}^{12}\text{C}$, ${}^{40}\text{Ca}$, ${}^{208}\text{Pb}(\vec{p}, \vec{n})$ reactions at $T_p = 346$ MeV and $\theta_{\text{lab}} = 22^\circ$. The solid and dashed curves are the ratios of the RPA and free response functions, respectively.

The close agreement in magnitude from the ${}^{12}\text{C}(\vec{p}, \vec{n})$ through ${}^{208}\text{Pb}(\vec{p}, \vec{n})$ results indicates that the target-mass dependence has been properly accounted for in calculations of the effective neutron number N_{eff} .

There are some sources of systematic uncertainties in the absolute magnitude of the experimental spin-response functions. In the present analysis, the absorption effect of nuclear distortions is treated by the effective neutron number N_{eff} . There is the uncertainty of about 10% in the calculation of N_{eff} , which directly affects the magnitude of the experimental spin response functions.

C. Ratio of spin-response functions

Much of the uncertainty associated with calculations of N_{eff} might be removed by taking the ratio of spin-response functions. The ratios R_L^-/R_T^- are displayed in Fig. 16. For ${}^{12}\text{C}$ and ${}^{40}\text{Ca}$, the solid curves are the theoretical ratios of the RPA response functions with $(g'_{NN}, g'_{N\Delta}, g'_{\Delta\Delta}) = (0.6, 0.3, 0.5)$ and $m^*(r=0) = 0.7m_N$, and the dashed curves represent the ratios of the free response functions with $m^*(r=0) = m_N$ [see Eq. (36)] [43,44]. A brief description of the RPA calculations will be presented in Sec. VIII. The observed ratios show no evidence for the theoretically expected enhancement of R_L^-/R_T^- . To within the experimental uncertainties of about ± 0.07 per 5-MeV (statistical) and ± 0.03 per 5-MeV (systematic), the R_L^-/R_T^- values are consistent with or smaller than unity.

The present results for R_L^-/R_T^- are consistent with the previous experimental studies of quasielastic (\vec{p}, \vec{p}') [16,17]

and (\vec{p}, \vec{n}) [21–23] reactions. The lack of the enhancement of R_L^-/R_T^- has been considered as evidence against the enhancement of the pionic modes [45–47]. However, as discussed below, this is too early to draw such a conclusion since signatures of the pionic enhancement in R_L^-/R_T^- are masked by the excess of R_T^- . This excess of R_T^- will be revealed by comparison of R_T^- of the (\vec{p}, \vec{n}) reaction to R_T^0 of the quasielastic electron scattering as well as to the RPA response function.

VII. COMPARISON TO ELECTRON SCATTERING

The spin-transverse response function deduced from the (\vec{p}, \vec{n}) reaction can be compared to that of the quasielastic electron scattering. In a one-photon-exchange PWBA, the laboratory-frame inclusive cross section $I^{ee'}$ of the quasielastic electron scattering can be described with the longitudinal (charge) S_L and transverse (spin and current) S_T response functions by the Rosenbluth formula as [48]

$$I^{ee'} = \frac{4\pi}{M_T} \sigma_{\text{Mott}} \eta C \left[\left(\frac{Q_\mu^2}{q_{\text{lab}}^2} \right)^2 S_L(q, \omega_{\text{int}}) + \left(\frac{Q_\mu^2}{2q_{\text{lab}}^2} + \tan^2 \frac{\theta_{\text{lab}}}{2} \right) S_T(q, \omega_{\text{int}}) \right], \quad (33)$$

where M_T is the target mass, σ_{Mott} is the Mott cross section, η is the recoil factor given in Ref. [49], C is the transformation factor given in Eq. (10), and Q_μ^2 is the 4-momentum transfer squared. The transverse response function S_T can be converted to R_T^0 of the quasielastic electron scattering per nucleon according to

$$\frac{4\pi}{M_T} S_T(q, \omega_{\text{int}}) = \frac{A}{2} \left(\frac{q}{2m_N} \right)^2 (\mu_n - \mu_p)^2 G_D^2(Q_\mu^2) R_T^0(q, \omega_{\text{int}}), \quad (34)$$

where $\mu_p = 2.79$, $\mu_n = -1.91$, and G_D is the empirical dipole form factor given by [50]

$$G_D(Q_\mu^2) = \left(1 + \frac{Q_\mu^2}{0.71 (\text{GeV}/c)^2} \right)^{-2}. \quad (35)$$

Note that Eq. (34) ignores isospin-mixing effects and the small contributions both of the isoscalar magnetic moment and of the convection current [51].

For ^{12}C , ^{40}Ca , ^{208}Pb , and ^{238}U , there are measurements which are closely match the present experiment for the momentum transfer. The Saclay group has reported the (e, e') spin-transverse response functions for ^{12}C [7], ^{40}Ca [8], and ^{208}Pb [9] at $q_{\text{lab}} = 1.8, 1.7,$ and 1.8 fm^{-1} (350, 330, and 350 MeV/c), respectively. We compared them with our (\vec{p}, \vec{n}) spin-transverse response functions in Fig. 17. The Bates group has also reported the (e, e') spin-transverse response functions for ^{40}Ca [11] at $q_{\text{lab}} = 1.7 \text{ fm}^{-1}$ (330 MeV/c) and ^{238}U [12] at $q_{\text{lab}} = 1.5$ and 2.0 fm^{-1} (300 and 400 MeV/c). They are also shown in Fig. 17. The R_T^0 values of ^{238}U averaged over those at $q_{\text{lab}} = 1.5$ and 2.0 fm^{-1} are shown in the open boxes for ^{208}Pb .

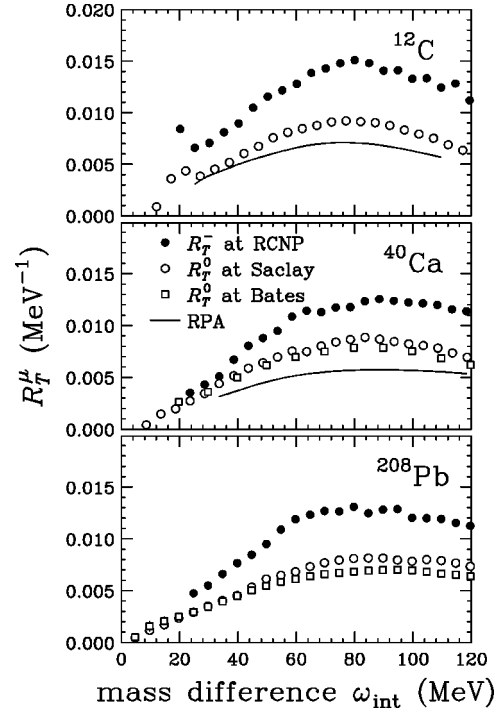


FIG. 17. The experimental spin-transverse response function R_T^- (filled circles) for the $^{12}\text{C}(\vec{p}, \vec{n})$ (top panel), $^{40}\text{Ca}(\vec{p}, \vec{n})$ (middle panel), and $^{208}\text{Pb}(\vec{p}, \vec{n})$ (bottom panel) reactions at $T_p = 346 \text{ MeV}$ and $\theta_{\text{lab}} = 22^\circ$ ($q_{\text{lab}} \approx 1.7 \text{ fm}^{-1}$). The open circles and the open boxes are R_T^0 of the quasielastic electron scattering by Saclay [7–9] and Bates [11,12] groups, respectively. The solid curves are the RPA response functions.

The (e, e') spin-transverse response functions deduced from the Saclay results are about 10% larger than those deduced from the Bates results for both ^{40}Ca and ^{208}Pb . The (\vec{p}, \vec{n}) spin-transverse response function agrees very well in shape with the corresponding (e, e') one, but it is larger in magnitude by factors of 1.5, 1.4, and 1.6 for ^{12}C , ^{40}Ca , and ^{208}Pb , respectively. The excess of the (\vec{p}, \vec{n}) spin-transverse response functions is significantly large beyond their uncertainties of about 10%. The origin of this excess will be discussed in Sec. IX by considering both the spin-direction dependence of N_{eff} and the two-step contribution.

The solid curves in Fig. 17 are the RPA response functions with $(g'_{NN}, g'_{N\Delta}, g'_{\Delta\Delta}) = (0.6, 0.3, 0.5)$ and $m^*(r=0) = 0.7m_N$ [43,44]. For both ^{12}C and ^{40}Ca , the (e, e') spin-transverse response function is larger than the corresponding RPA one. The discrepancy would be due to MEC and nuclear correlations beyond RPA such as the $2p2h$ configuration mixing [51–55]. The differences between (\vec{p}, \vec{n}) , (e, e') , and RPA spin-response functions will be discussed in Sec. X.

VIII. COMPARISON TO RPA RESPONSE FUNCTIONS

The implication of the present data can be further emphasized by comparing to the theoretical response functions. The spin-response functions are calculated in a framework of RPA [43,44], in which the continuum RPA method [56] with the orthogonality condition [57,58] is used to treat nuclear

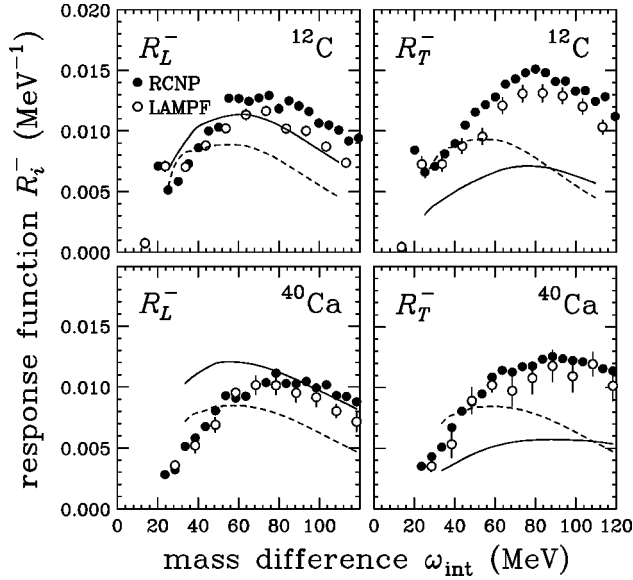


FIG. 18. The experimental spin-longitudinal R_L^- (left panels) and spin-transverse R_T^- (right panels) response functions for the $^{12}\text{C}(\bar{p}, \bar{n})$ (upper panels) and $^{40}\text{Ca}(\bar{p}, \bar{n})$ (lower panels) reactions at $T_p = 346$ MeV and $\theta_{\text{lab}} = 22^\circ$ ($q_{\text{lab}} \approx 1.7$ fm $^{-1}$). The solid and dashed curves are the RPA and free response functions, respectively. The open circles represent the spin-response functions from the LAMPF data [22,23].

finite-size effects. The virtual excitation of Δ is included, and the $\pi + \rho + g'$ model [1] is adopted for the p - h and Δ - h residual interaction. The calculations are performed without the commonly used universality ansatz ($g'_{NN} = g'_{N\Delta} = g'_{\Delta\Delta}$), namely we treat all of the g 's independently. The mean field of the finite nucleus is represented by a Woods-Saxon (WS) potential. The nonlocality of the mean field is treated by an effective mass m^* with radial dependence of

$$m^*(r) = m_N - \frac{f_{\text{WS}}(r)}{f_{\text{WS}}(0)} [m_N - m^*(0)], \quad (36)$$

in which f_{WS} is the WS radial form factor. The spreading widths of the particle and of the hole states are taken into account by the imaginary potential and by the complex binding energy, respectively.

Figure 18 compares the experimental spin-longitudinal R_L^- and spin-transverse R_T^- response functions for ^{12}C and ^{40}Ca with the theoretical spin-response functions. The solid curves are the results of RPA calculations with $(g'_{NN}, g'_{N\Delta}, g'_{\Delta\Delta}) = (0.6, 0.3, 0.5)$ and $m^*(0) = 0.7m_N$, and the dashed curves represent the free response functions with $m^*(0) = m_N$. These g 's and m^* have been determined [40] by DWIA calculations to reproduce the experimental spin-longitudinal cross section for ^{12}C deduced from the LAMPF data [22,23]. The spin-response functions extracted from the LAMPF data are also shown by the open circles in Fig. 18. The present spin-response functions for ^{12}C are slightly larger than those of the LAMPF measurement, while the spin-response functions for ^{40}Ca are consistent with each other. Since experimental spin-response functions have the uncertainty of about 10%, the difference for ^{12}C is not significant.

In the spin-longitudinal mode, the theoretically expected enhancement is clearly observed for both ^{12}C and ^{40}Ca . The observed enhancement of R_L^- from the free-response function is beyond the uncertainty of the experimental response functions of about 10%. The experimental response function for ^{12}C is in fairly good agreement with the RPA result in shape, while that for ^{40}Ca is substantially hardened compared to the RPA result. The position of the quasielastic peak is affected by m^* . In a Fermi gas model, the peak position is given by $q^2/2m^*$. Furthermore, as discussed in the next section, the shape of the experimental response function is affected by using the spin-dependent effective neutron number. Thus it is very difficult to conclude whether the theoretically predicted softening is observed experimentally or not.

In the spin-transverse mode, for both ^{12}C and ^{40}Ca , the experimental response functions are significantly larger than the RPA results and even larger than the free-response functions, namely R_T^- is enhanced contradicting with the theoretical prediction, i.e., quenching. This large excess of R_T^- masks possible signatures of the pionic enhancement in R_L^-/R_T^- .

IX. COMPARISON TO DWIA CALCULATIONS

The most important effect of nuclear distortions is the absorption. Up to the previous section, this effect has been treated by the effective neutron number N_{eff} independent of the spin direction. The spin-direction-dependent $N_{i;\text{eff}}$ is evaluated by comparing the results of DWIA and PWIA calculations as [40]

$$N_{i;\text{eff}}(\omega_{\text{lab}}) = N \frac{ID_i^{\text{DW}}(\omega_{\text{lab}})}{ID_i^{\text{PW}}(\omega_{\text{lab}})}, \quad (i=q \text{ or } p), \quad (37)$$

where N is the target neutron number, and ID_i^{DW} and ID_i^{PW} are the polarized cross sections in DWIA and PWIA calculations, respectively. The formalism of DWIA calculations is described in Refs. [15,59,60]. The calculations were performed for ^{12}C and ^{40}Ca .

Figure 19 compares the experimental polarized cross sections ID_q and ID_p with the DWIA+RPA calculations. The solid curves are the results of DWIA calculations with the RPA response functions employing $(g'_{NN}, g'_{N\Delta}, g'_{\Delta\Delta}) = (0.6, 0.3, 0.5)$ and $m^*(0) = 0.7m_N$. The dashed curves are the DWIA results with the free-response functions employing $m^*(0) = m_N$. These results have been normalized by 1.06 and 1.17 for ID_q and ID_p , respectively. These normalization factors are the same as those required to reproduce the experimental spin-response functions for ^2H by the theoretical calculations.

In the energy-transfer region of $\omega_{\text{lab}} = 40 - 120$ MeV, if we use the results with RPA correlations, the spin-direction-dependent $N_{i;\text{eff}}$ values obtained from Eq. (37) become $N_{q;\text{eff}} = 2.4 - 2.6$ and $N_{p;\text{eff}} = 2.7 - 3.2$ for ^{12}C , and $N_{q;\text{eff}} = 3.9 - 4.3$ and $N_{p;\text{eff}} = 5.9 - 7.1$ for ^{40}Ca . Note that the spin-direction dependence of the N_{eff} values comes from both the effects of the spin-orbit part of the optical potential and the difference of the radial dependence between the spin-longitudinal and spin-transverse response functions. The spin-direction dependence for ^{12}C is rather small with

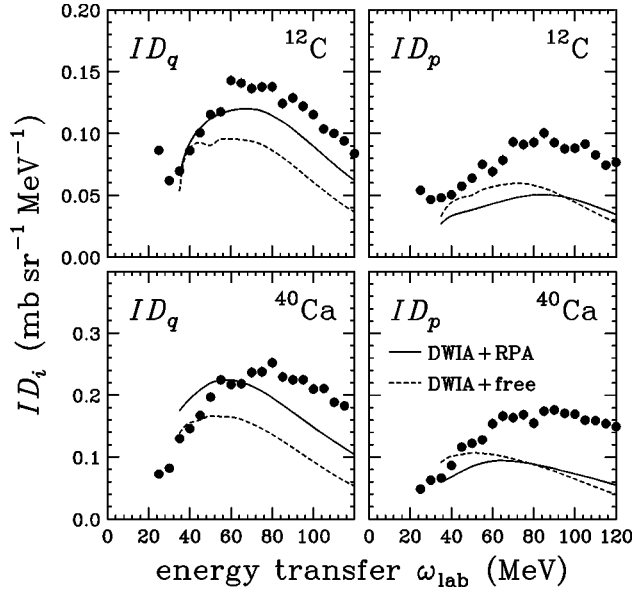


FIG. 19. The spin-longitudinal ID_q (left panels) and spin-transverse ID_p (right panels) polarized cross sections for the $^{12}\text{C}(\vec{p}, \vec{n})$ (upper panels) and $^{40}\text{Ca}(\vec{p}, \vec{n})$ (lower panels) reactions at $T_p = 346$ MeV and $\theta_{\text{lab}} = 22^\circ$ ($q_{\text{lab}} \approx 1.7$ fm $^{-1}$). The solid and dashed curves represent the results of DWIA calculations with RPA and free response functions, respectively. The results of DWIA calculations have been normalized by factors of $N_q = 1.06$ and $N_p = 1.17$ for ID_q and ID_p , respectively. See text for details.

9–22% in this region, and the spin-direction-dependent $N_{i;\text{eff}}$ values are close to the spin-direction-independent N_{eff} values of 2.5–2.7 obtained in the eikonal approximation. On the contrary, the spin-direction dependence for ^{40}Ca is significantly larger with 31–43%. The N_{eff} values in the eikonal approximation are 5.4–5.8 in this region. Thus, if we use the spin-direction-dependent $N_{i;\text{eff}}$ values, the spin-longitudinal response function for ^{40}Ca becomes 27–48% larger than that shown in Fig. 18, while the spin-transverse response function becomes 2–23% smaller.

The DWIA+RPA calculations could reproduce ID_q fairly well for both ^{12}C and ^{40}Ca at the low-energy-transfer region of $\omega_{\text{lab}} \leq 60$ MeV, while they fail to reproduce ID_q at the high-energy-transfer region of $\omega_{\text{lab}} > 60$ MeV. The calculations underestimate ID_p by a factor of 2 or so in the quasielastic region. The disagreement between experimental and theoretical results at the high-energy-transfer region might suggest the importance of the two-step contribution in this region.

Recently, Nakaoka [61] has pointed out that the two-step contribution for ID_p would be significantly larger than that for ID_q . In the two-step process, the momentum transfers of the first and second steps share the experimentally observed momentum transfer $q \approx 1.7$ fm $^{-1}$. Thus the two-step contribution can be represented as a coherent sum of the contributions with various combinations of the first and second step momentum transfers. In the momentum-transfer region from 0 to $q \approx 1.7$ fm $^{-1}$, the spin-longitudinal interaction changes its sign at around 0.7 fm $^{-1}$, while the spin-transverse interaction remains positive (repulsive). Thus the coherent sum for ID_q is partly destructive, while that for ID_p is wholly constructive. As a result, the two-step contribution for ID_p is

more important than that for ID_q . The two-step contribution for ID_p would be partly responsible for the discrepancy of the (\vec{p}, \vec{n}) spin-transverse response function from the corresponding (e, e') and RPA ones.

X. REMARKS ON COMPARISON OF VARIOUS RESPONSE FUNCTIONS

At the end we discuss the differences between (\vec{p}, \vec{n}) , (e, e') , and RPA spin-response functions in more detail. The experimental spin-response functions represent not only the RPA correlation treated here, but also the effects of the higher-order (such as $2p2h$) configuration mixing, etc. Further the (e, e') spin-transverse response function includes the contribution of MEC which is absent in the (\vec{p}, \vec{n}) one. Carlson and Schiavilla [54] estimated the contribution of MEC to the (e, e') spin-transverse response function R_T^0 to be more than 20%, while Suzuki [52] predicted it to be only a few percents. Alberico *et al.* [51] and Adams and Castel [55] claimed that the $2p2h$ contribution significantly increases R_T^0 around the quasielastic peak. However, Takayanagi [53] criticized the calculation of Alberico *et al.* [51] because it does not exhaust all of the second-order perturbation diagrams, and showed that the full second-order processes reduce the response functions around the quasielastic peak at the present momentum-transfer region. Considering these situations, we must say that it is still an open question whether the difference between the (e, e') and RPA spin-transverse response functions can be understood by taking account of the higher-order configuration mixing and MEC.

Here we set a simple model and consider the two extreme cases. We first assume the experimental spin-response functions are expressed as

$$R_L^-(\vec{p}, \vec{n}) = R_L^{-;\text{RPA}} + R_L^{-;2p2h} + R_L^{-;2\text{-step}}, \quad (38a)$$

$$R_T^-(\vec{p}, \vec{n}) = R_T^{-;\text{RPA}} + R_T^{-;2p2h} + R_T^{-;2\text{-step}}, \quad (38b)$$

$$R_T^0(e, e') = R_T^{0;\text{RPA}} + R_T^{0;2p2h} + R_T^{0;\text{MEC}}, \quad (38c)$$

where $R_i^{\mu;\text{RPA}}$, $R_i^{\mu;2p2h}$, $R_i^{\mu;2\text{-step}}$, and $R_i^{0;\text{MEC}}$ denote the RPA, $2p2h$, two-step, and MEC contributions, respectively. We neglect the isospin-transfer dependence ($R_i^- = R_i^0$) and further assume that $R_L^{-;2p2h} \approx R_T^{-;2p2h} \approx R_T^{0;2p2h}$. As was mentioned in the previous section, $R_L^{-;2\text{-step}}$ would be small around the quasielastic peak and we set it to zero in the present model.

The first extreme case is that the difference between (e, e') and RPA spin-transverse response functions is only due to MEC, namely the $2p2h$ configuration mixing is negligible. Then we could directly compare $R_L^-(\vec{p}, \vec{n})$ to $R_L^{-;\text{RPA}}$ as we did in this paper. We confirmed the enhancement of R_L^- in this limiting case.

The second extreme is that the difference is only due to the $2p2h$ contribution, and hence $R_T^{0;\text{MEC}}$ is negligible. Then it may be useful to consider the difference

$$R_L^-(\vec{p}, \vec{n}) - R_T^0(e, e') \approx R_L^{-;\text{RPA}} - R_T^{0;\text{RPA}} \approx R_L^{-;\text{RPA}} - R_T^{-;\text{RPA}}, \quad (39)$$

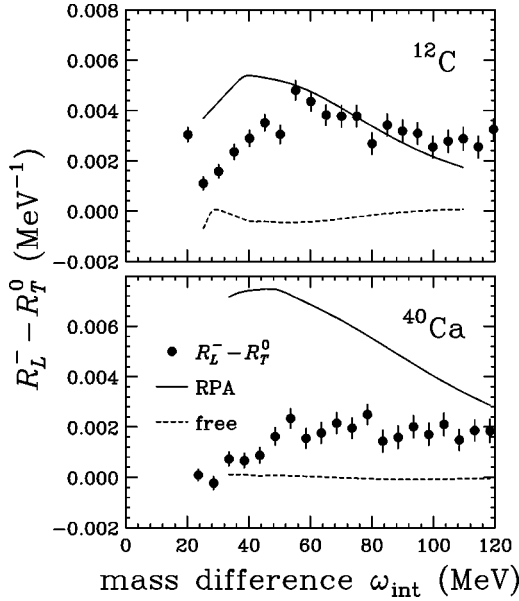


FIG. 20. The difference between the (\vec{p}, \vec{n}) spin-longitudinal R_L^- and the (e, e') spin-transverse R_T^0 response functions for ^{12}C (upper panel) and ^{40}Ca (lower panel). The solid and dashed curves are the results of the RPA and free response functions, respectively.

in order to see the RPA contributions exclusively.

Figure 20 compares the experimental observable $R_L^-(\vec{p}, \vec{n}) - R_T^0(e, e')$ to the theoretical values of $R_L^- - R_T^-$. Here the Saclay data are used for $R_T^0(e, e')$. The solid and dashed curves, respectively, denote the RPA results and those of the free-response functions shown in Sec. VIII.

A reasonable agreement between the experimental and RPA results is obtained for ^{12}C , but the experimental values are smaller than those of RPA for ^{40}Ca . However, if we use the spin-direction-dependent $N_{i;\text{eff}}$ for ^{40}Ca shown in the previous section, $R_L^-(\vec{p}, \vec{n})$ becomes larger by 30–54%, and we get better agreement. The contribution of MEC and the difference between $R_L^-:2p2h(\vec{p}, \vec{n})$ and $R_T^0:2p2h(e, e')$, which are neglected in the present model, might also be responsible for the disagreement.

The observed agreement supports the conclusion that our experimental data strongly imply the pionic enhancement of R_L^- in this second extreme, too. Of course, the theoretical works for the spin-response functions with the full contributions of the higher-order configuration mixing and MEC and reliable estimation of the contribution of the two-step processes should be called for to understand the difference between (\vec{p}, \vec{n}) , (e, e') , and RPA spin-response functions quantitatively.

XI. SUMMARY

In summary, the cross section, analyzing power, induced polarization, and polarization transfer coefficients for quasi-elastic (\vec{p}, \vec{n}) reactions on ^2H , ^6Li , ^{12}C , ^{40}Ca , and ^{208}Pb have been measured at $T_p = 346$ MeV and $\theta_{\text{lab}} = 22^\circ$ ($q_{\text{lab}} \approx 1.7$ fm $^{-1}$).

The experimental spin-longitudinal R_L^- and spin-transverse R_T^- response functions are extracted within a

framework of PWIA with eikonal and optimal factorization approximations. The experimentally obtained R_L^-/R_T^- values show no evidence for the theoretically expected enhancement. The observed values are consistent with or smaller than unity within the uncertainties of about ± 0.07 per 5-MeV (statistical) and ± 0.03 per 5-MeV (systematic). The present results for R_L^-/R_T^- confirm the results of the previous studies of quasielastic (\vec{p}, \vec{p}') and (\vec{p}, \vec{n}) reactions which reveal no evidence for an enhancement of R_L^-/R_T^- at a momentum transfer where the enhancement should be largest. However, the lack of the enhancement of R_L^-/R_T^- does not necessarily mean the absence of the pionic enhancement of R_L^- .

The spin-transverse response function of the (\vec{p}, \vec{n}) reaction agrees well in shape with that of the (e, e') reaction, but it is significantly larger in magnitude by factors of 1.5, 1.4, and 1.6 for ^{12}C , ^{40}Ca , and ^{208}Pb , respectively. The uncertainty of the (\vec{p}, \vec{n}) spin-response functions associated with the effective neutron number N_{eff} is estimated to be about 10%. Thus the deviation between the (\vec{p}, \vec{n}) and (e, e') results is substantially larger than this uncertainty. This apparent excess of R_T^- is responsible for masking possible signatures of the pionic enhancement in R_L^-/R_T^- .

The spin-response functions for ^{12}C and ^{40}Ca are compared to RPA response functions. In the spin-longitudinal mode, the theoretically expected enhancement is clearly observed for both ^{12}C and ^{40}Ca . The observed enhancement of R_L^- from the free-response function is significantly large compared to the uncertainty of the experimental spin-response functions of about 10%. In the spin-transverse mode, the experimental R_T^- agrees fairly well in shape with the RPA result which predicts the hardening of R_T^- with respect to the free response function. However, it is substantially larger than the RPA calculation for both ^{12}C and ^{40}Ca .

The N_{eff} values depend on the spin direction because of both the effects of the spin-orbit potential and the difference of the radial dependence between the spin-response functions. The spin-direction dependence of N_{eff} is examined by comparing the results of DWIA and PWIA calculations with RPA response functions. The spin-direction-dependent $N_{i;\text{eff}}$ become $N_{q;\text{eff}} = 2.4 - 2.6$ and $N_{p;\text{eff}} = 2.7 - 3.2$ for ^{12}C , and $N_{q;\text{eff}} = 3.9 - 4.3$ and $N_{p;\text{eff}} = 5.9 - 7.1$ for ^{40}Ca in the energy-transfer region of $\omega_{\text{lab}} = 40 - 120$ MeV. These values should be compared to the spin-direction-independent N_{eff} in the eikonal approximation of 2.5–2.7 for ^{12}C and 5.4–5.8 for ^{40}Ca in the same region. The spin-direction-dependence for ^{12}C is rather small with 9–22%, while that for ^{40}Ca is large with 31–43%. Thus, by using the spin-direction-dependent $N_{i;\text{eff}}$, R_L^- for ^{40}Ca is more enhanced by 27–48%, while R_T^- becomes small by 2–23%.

In the (\vec{p}, \vec{n}) reaction, the two-step contribution is expected to be more important for the spin-transverse ID_p polarized cross section than for the spin-longitudinal ID_q one. Thus the excess of the (\vec{p}, \vec{n}) spin-transverse response function compared to the corresponding (e, e') one would be due to both the two-step contribution to ID_p and the overestimation of R_T^- originating from the use of N_{eff} independent of the spin direction. The present RPA spin-response function is

composed only of RPA correlation. Therefore, the theoretical works for the spin-response function including the effect of the higher-order configuration mixing as well as for the reaction mechanism including the two-step process employing the realistic spin-response function should be called for to investigate the difference between (\vec{p}, \vec{n}) , (e, e') , and RPA spin-response functions quantitatively.

ACKNOWLEDGMENTS

We are grateful to K. Nishida, A. Itabashi, and Y. Nakaoka for their helpful correspondence. We also thank Pro-

fessor H. Ejiri, Director of RCNP, for his continuous encouragement throughout the work, and the RCNP cyclotron crew for their efforts in providing a good quality polarized proton beam. The experiment was performed at RCNP under Program Number E59. This work was supported in part by the Grants-in-Aid for Scientific Research Nos. 6342007, 05640328, 07304030, 08454056, and 10304018 of the Ministry of Education, Science, Sports and Culture of Japan. T.W. would like to also acknowledge the partial support by a Grant-in-Aid from the Japan Society for the Promotion of Science (JSPS) of the Ministry of Education, Science, Sports and Culture of Japan.

-
- [1] W. M. Alberico, M. Ericson, and A. Molinari, *Nucl. Phys.* **A379**, 429 (1982).
- [2] C. H. Llewellyn Smith, *Phys. Lett.* **128B**, 107 (1983).
- [3] M. Ericson and A. W. Thomas, *Phys. Lett.* **128B**, 112 (1983).
- [4] B. L. Friman, V. R. Pandharipande, and R. B. Wiringa, *Phys. Rev. Lett.* **51**, 763 (1983).
- [5] E. L. Berger, F. Coester, and R. B. Wiringa, *Phys. Rev. D* **29**, 398 (1984).
- [6] D. Stump, G. F. Bertsch, and J. Pumlin, in *Hadron Substructure in Nuclear Physics*, edited by W-Y P. Hwang *et al.*, AIP Conf. Proc. 110 (AIP, New York, 1984) 339.
- [7] P. Barreau *et al.*, *Nucl. Phys.* **A402**, 515 (1983); P. Barreau *et al.*, Centre d'Etudes Nucléaires de Saclay Report No. CEA-N-2334, 1983 (unpublished).
- [8] Z. E. Meziani *et al.*, *Phys. Rev. Lett.* **54**, 1233 (1985).
- [9] A. Zghiche *et al.*, *Nucl. Phys.* **A572**, 513 (1994).
- [10] M. Deady *et al.*, *Phys. Rev. C* **28**, 631 (1983).
- [11] M. Deady, C. F. Williamson, P. D. Zimmerman, R. Altemus, and R. R. Whitney, *Phys. Rev. C* **33**, 1897 (1986).
- [12] C. C. Blatchley, J. J. Lerosé, O. E. Pruet, Peter D. Zimmerman, C. F. Williamson, and M. Dadey, *Phys. Rev. C* **34**, 1243 (1986).
- [13] C. F. Williamson *et al.*, *Phys. Rev. C* **56**, 3152 (1997).
- [14] W. M. Alberico, A. De Pace, M. Ericson, Mikkel B. Johnson, and A. Molinari, *Phys. Rev. C* **38**, 109 (1988).
- [15] M. Ichimura, K. Kawahigashi, T.S. Jørgensen, and C. Gaarde, *Phys. Rev. C* **39**, 1446 (1989).
- [16] T. A. Carey, K. W. Jones, J. B. McClelland, J. M. Moss, L. B. Rees, N. Tanaka, and A. D. Bacher, *Phys. Rev. Lett.* **53**, 144 (1984).
- [17] L. B. Rees, J. M. Moss, T. A. Carey, K. W. Jones, J. B. McClelland, N. Tanaka, A. D. Bacher, and H. Esbensen, *Phys. Rev. C* **34**, 627 (1986).
- [18] R. Fergerson, J. McGill, C. Glashauser, K. Jones, S. Nanda, Sun Zuxun, M. Barlett, G. Hoffmann, J. Marshall, and J. McClelland, *Phys. Rev. C* **38**, 2193 (1988).
- [19] O. Häusser *et al.*, *Phys. Rev. Lett.* **61**, 822 (1988).
- [20] C. Chan *et al.*, *Nucl. Phys.* **A510**, 713 (1990).
- [21] J. B. McClelland *et al.*, *Phys. Rev. Lett.* **69**, 582 (1992).
- [22] X. Y. Chen *et al.*, *Phys. Rev. C* **47**, 2159 (1993).
- [23] T. N. Taddeucci *et al.*, *Phys. Rev. Lett.* **73**, 3516 (1994).
- [24] H. Sakai, H. Okamura, H. Otsu, T. Wakasa, S. Ishida, N. Sakamoto, T. Uesaka, Y. Satou, S. Fujita, and K. Hatanaka, *Nucl. Instrum. Methods Phys. Res. A* **369**, 120 (1996).
- [25] H. Sakai, H. Okamura, S. Ishida, K. Hatanaka, and T. Noro, *Nucl. Instrum. Methods Phys. Res. A* **320**, 479 (1992).
- [26] T. Wakasa *et al.*, *Nucl. Instrum. Methods Phys. Res. A* **404**, 355 (1998).
- [27] K. Hatanaka, K. Takahisa, H. Tamura, H. Kaneko, and I. Miura, *Nucl. Instrum. Methods Phys. Res. A* **384**, 575 (1997).
- [28] T. N. Taddeucci *et al.*, *Phys. Rev. C* **41**, 2548 (1990).
- [29] D. V. Bugg and R. A. Bryan, phase-shift solution parametrized in the SAID program of Arndt and Roper, dated 1992.
- [30] R. A. Arndt and L. D. Roper, *Scattering Analysis Interactive Dial-In program* (SAID), phase-shift solution SP98, Virginia Polytechnic Institute and State University (unpublished).
- [31] M. Ichimura and K. Kawahigashi, *Phys. Rev. C* **45**, 1822 (1992).
- [32] See AIP Document No. E-PRVCAN-59-023906 for the data presented in Figs. 3–8. E-PAPS document files may be retrieved free of charge from our FTP server (<http://www.aip.org/epaps/epaps.html>) or from <ftp.aip.org> in the directory /epaps/. For further information, email: pap@aip.org; or fax: 516-576-2223.
- [33] E. Bleszynski, M. Bleszynski, and C. A. Whitten, Jr., *Phys. Rev. C* **26**, 2063 (1982).
- [34] M. Ichimura, in *Proceedings of the RCNP International mini Workshop on Nuclear Medium Effect via Nucleon Induced Reaction*, Kyoto, 1997, edited by H. Sakai, H. Sakaguchi, and T. Noro (Genshikaku Kenkyu, Tokyo, 1997), p. 21.
- [35] A. K. Kerman, H. McManus, and R. M. Thaler, *Ann. Phys. (N.Y.)* **8**, 551 (1959).
- [36] N. Hoshizaki, *Prog. Theor. Phys. Suppl.* **42**, 107 (1968).
- [37] C. W. de Jager, H. de Vries, and C. de Vries, *At. Data Nucl. Data Tables* **14**, 479 (1974).
- [38] R. D. Smith and M. Bozoian, *Phys. Rev. C* **39**, 1751 (1989).
- [39] H. Sakai *et al.*, *Nucl. Phys.* **A577**, 111c (1994).
- [40] M. Ichimura, K. Nishida, A. Itabashi, and K. Kawahigashi, in *Proceedings of the 6th International Spring Seminar on Nuclear Physics*, S. Agata Sui Due Golfi, 1998, edited by A. Covello (World Scientific, Singapore, in press).
- [41] A. Itabashi, K. Aizawa, and M. Ichimura, *Prog. Theor. Phys.* **91**, 69 (1994).
- [42] S. A. Dytman, A. M. Bernstein, K. I. Blomqvist, T. J. Pavel, B. P. Quinn, R. Altemus, J. S. McCarthy, G. H. Mechtel, T. S. Ueng, and R. R. Whitney, *Phys. Rev. C* **38**, 800 (1988).
- [43] K. Nishida and M. Ichimura, *Phys. Rev. C* **51**, 269 (1995).
- [44] A. Itabashi, Ph.D. thesis, University of Tokyo, 1996.

- [45] G. F. Bertsch, L. Frankfurt, and M. Strikman, *Science* **259**, 773 (1993).
- [46] G. E. Brown, M. Buballa, Zi Bang Li, and J. Wambach, *Nucl. Phys.* **A593**, 295 (1995).
- [47] D. S. Koltun, *Phys. Rev. C* **57**, 1210 (1998).
- [48] T. W. Donnelly and J. D. Walecka, *Annu. Rev. Nucl. Sci.* **25**, 329 (1975).
- [49] J. P. Glickman *et al.*, *Phys. Rev. C* **43**, 1740 (1991).
- [50] P. Markowitz *et al.*, *Phys. Rev. C* **48**, R5 (1993).
- [51] W. M. Alberico, M. Ericson, and A. Molinari, *Ann. Phys. (N.Y.)* **154**, 356 (1984).
- [52] T. Suzuki, *Nucl. Phys.* **A495**, 581 (1989).
- [53] K. Takayanagi, *Nucl. Phys.* **A516**, 276 (1990).
- [54] J. Carlson and B. Schiavilla, *Phys. Rev. C* **49**, R2880 (1994).
- [55] J. P. Adams and B. Castel, *Phys. Rev. C* **50**, R1763 (1994).
- [56] S. Shlomo and G. F. Bertsch, *Nucl. Phys.* **A243**, 507 (1975).
- [57] T. Izumoto and A. Mori, *Phys. Lett.* **82B**, 163 (1979).
- [58] T. Izumoto, *Nucl. Phys.* **A395**, 189 (1983).
- [59] K. Kawahigashi, Ph.D. thesis, University of Tokyo, 1989.
- [60] K. Nishida, Ph.D. thesis, University of Tokyo, 1995.
- [61] Y. Nakaoka, M.S. thesis, University of Tokyo, 1996; (private communication).